Chandra and *XMM-Newton* observations of NGC 6251

D. A. Evans[1][*], M. J. Hardcastle[1,2], J. H. Croston[1,3], D. M. Worrall[1], and M. Birkinshaw[1]

[1] *Department of Physics, University of Bristol, Royal Fort, Tyndall Avenue, Bristol BS8 1TL, UK*
[2] *School of Physics, Astronomy & Mathematics, University of Hertfordshire, College Lane, Hatfield AL10 9AB, UK*
[3] *Service d'Astrophysique, CEA Saclay, L'Orme des Merisiers, 91191 Gif-sur-Yvette, France*

ABSTRACT

We present new X-ray observations of the nucleus, jet and extended emission of the nearby radio galaxy NGC 6251 using the *Chandra*/ACIS-S camera, together with a reanalysis of archival *Chandra*/ACIS-I and *XMM-Newton*/EPIC data. We find that the nuclear X-ray spectrum is well-fitted with an absorbed power-law, and that there is tentative, but not highly significant, evidence for Fe Kα emission. We argue that the observed nuclear X-ray emission is likely to originate in a relativistic jet, based on the double-peaked nature, and our synchrotron self-Compton modelling, of the radio-to-X-ray spectral energy distribution. However, we cannot rule out a contribution from an accretion flow. We resolve X-ray jet emission in three distinct regions, and argue in favour of a synchrotron origin for all three; inverse-Compton emission models are possible but require extreme parameters. We detect thermal emission on both galaxy and group scales, and demonstrate that hot gas can confine the jet, particularly if relativistic beaming is important. We show evidence that the radio lobe has evacuated a cavity in the X-ray-emitting gas, and suggest that the lobe is close to the plane of the sky, with the jet entering the lobe close to the surface nearest to the observer.

Key words: galaxies: active - galaxies: individual (NGC 6251) - galaxies: jets - X-rays: galaxies

1 INTRODUCTION

NGC 6251 is a nearby ($z = 0.0244$) Fanaroff Riley type I (FRI) radio galaxy with a supermassive black hole of mass $(4–8) \times 10^8$ M$_\odot$ (Ferrarese & Ford 1999). It exhibits complex morphology on a range of angular scales, and shows a rich variety of structure across the electromagnetic spectrum. Optically, NGC 6251 hosts a well-defined dust disk of diameter 730 pc for (H$_0$ = 70 km s^{-1} Mpc^{-1}) (Ferrarese & Ford 1999) and, based on velocity widths of allowed and forbidden lines, has been classified as a Seyfert 2 galaxy (Shuder & Osterbrock 1981). NGC 6251 is the parent galaxy of a spectacular radio jet, which extends 4.5 arcmin (130 kpc) north-west (NW) of the nucleus and has an opening angle of 7.4° (Waggett, Warner, & Baldwin 1977; Perley, Bridle, & Willis 1984). On smaller (milliarcsecond) scales, VLBI observations (e.g., Jones et al. 1986) have detected radio emission from an unresolved core, and a parsec-scale jet extending to the NW of the nucleus. A detection of a parsec-scale counterjet was claimed by Sudou et al. (2000), but disputed by Jones & Wehrle (2002), who placed a lower limit of 128 on the jet/counterjet brightness ratio, implying an angle to the line of sight $\theta < 40°$. VLA spectral-line radio observations of the inner regions of NGC 6251 (Werner 2002) show 21-cm neutral hydrogen absorption, corresponding to an intrinsic column

of $N_{\rm H}= (4.5^{+2.6}_{-2.4}) \times 10^{20}$ atoms cm^{-2}. At higher energies, it has been claimed that NGC 6251 is associated with the *CGRO*/EGRET gamma-ray source 3EG J1621 + 8203 (Mukherjee et al. 2002; Foschini et al. 2004).

X-ray emission from NGC 6251 was first detected with *ROSAT* (Birkinshaw & Worrall 1993), and has more recently been imaged in detail with *Chandra* and *XMM-Newton*. Birkinshaw & Worrall (1993) presented *ROSAT* PSPC observations of NGC 6251, detecting nuclear emission and a contribution from a hot, X-ray emitting halo. They argued that the kiloparsec-scale radio jet cannot be confined by gas pressure alone. Mack, Kerp, & Klein (1997a) reanalysed the *ROSAT* data, and confirmed the presence of an elliptically-shaped thermal X-ray halo extending out to $\sim$ 100 kpc, reporting enhanced X-ray emission coincident with components of the radio jet on 100-kpc scales. X-ray emission from the inner jet of NGC 6251 was imaged by Hardcastle & Worrall (1999) using the *ROSAT* HRI. Kerp & Mack (2003) used a *Chandra*/ACIS-I observation of NGC 6251 to argue that the pressure of the extended halo is sufficient to confine the radio jet. Their observation also confirmed the PSPC detection of the outer X-ray components of the jet. A subsequent *XMM-Newton* EPIC observation of the halo (Sambruna et al. 2004) measured a temperature for the gas of kT = 1.6 keV. The *XMM-Newton* spectrum of the outer regions of the X-ray jet ruled out a thermal model for the X-radiation, and Sambruna et al. (2004) argued that

[*] Email: D.A.Evans@bristol.ac.uk

arXiv:astro-ph/0502183v2   6 Mar 2005

the emission was due to beamed inverse-Compton scattering of cosmic microwave background (CMB) photons to X-ray energies.

The physical origin of the nuclear X-ray continuum of NGC 6251, as with other radio galaxies, is uncertain. Two popular interpretations for the origin of the emission are: (1) accretion phenomena in or near a disk; and (2) nonthermal processes (inverse-Compton or synchrotron emission) in a subparsec-scale jet. The first model is often supported by the detection of high equivalent width Fe Kα lines. The second interpretation is supported for radio galaxies in general by the observed correlation between the luminosities of soft, unresolved X-ray emission and 5-GHz core radio emission (e.g., Worrall & Birkinshaw 1994; Canosa et al. 1999; Hardcastle & Worrall 1999). The nuclear spectrum of NGC 6251, as measured with *ASCA* (Turner et al. 1997) and *XMM-Newton* (Gliozzi et al. 2004), was modelled with a power law and a high equivalent width fluorescent Fe Kα emission line, suggesting that the X-ray emission originates from an accretion flow. However, the power-law continuum measured with BeppoSAX (Guainazzi et al. 2003) had a somewhat flatter photon index and higher luminosity than the earlier *ASCA* observation in particular, with no Fe Kα line detected. Moreover, the double-peaked SED measured by, for example, Guainazzi et al. (2003), Ho (1999), and Chiaberge et al. (2003), led those authors to suggest that the dominant X-ray-production mechanism was synchrotron self-Compton (SSC) emission from a jet.

This paper is organised as follows. Section 2 contains a description of the data and a summary of our analysis. The results from our analysis of the nucleus, jet, and extended emission are presented in Section 3, and are discussed in Section 4. We end with our conclusions in Section 5. All results presented in this paper use a cosmology in which $\Omega_{m,0} = 0.3$ and $\Omega_{\Lambda,0} = 0.7$, and $H_0 = 70$ km s^{-1} Mpc^{-1}. At the redshift of NGC 6251 ($z = 0.0244$), 1 arcsec corresponds to 485 pc . All spectral fits include absorption through our Galaxy using $N_{H,Gal} = 5.82 \times 10^{20}$ atoms cm^{-2} (Murphy et al. 1996). When distinguishing between different model fits to the data, we present F-statistic results for ease of comparison with other papers, although we note that this method may be unreliable in such circumstances (Protassov et al. 2002). We adopt thresholds of 95 and 99.9 per cent for marginally and highly significant improvements in the fit, respectively. Errors quoted in this paper are 90 per cent confidence for one parameter of interest (i.e., $\chi^2_{min} + 2.7$), unless otherwise stated.

2 OBSERVATIONS AND ANALYSIS METHODS

2.1 Chandra

NGC 6251 was observed on 2003 November 11 (ObsID 4130) with the S3 and S4 chips of the *Chandra*/ACIS charge-coupled devide (CCD) camera. The observation was made in the VFAINT mode, using a 128-row subarray (giving a 1×16 arcmin field of view), in order to reduce the CCD frame time to 0.54 s and lessen the effect of pileup. The data were reprocessed using *CIAO v3.0.2* with the *CALDB* v2.26 calibration database to create a new level-2 events file with grades 0, 2, 3, 4, 6, afterglow events preserved, and the 0.5-arcsec pixel randomization removed. To check for intervals of high particle background, light curves were extracted for the ACIS-S3 chip, excluding the core. Inspection of the light curves revealed the presence of several flares which were removed from our analysis, reducing the total exposure time from 46.5 ks to 43.0 ks.

The *Chandra* observation of the nucleus of NGC 6251 is piled

up. We demonstrate this using two independent methods. First, the counts extracted from a source-centred circle of radius 1.23 arcsec (2.5 pixels) in the 0.5–7 keV energy band gave 0.35 counts per frame exposure time, for which a pileup fraction of $\sim$ 10–15 per cent is predicted using the PIMMS software. As a second independent test, we estimated the spatial extent of the pileup by producing an image consisting of 'afterglow' events, which are produced from residual charges from either cosmic-ray events or from piled-up events. We computed the numbers of afterglow events per unit area within two extraction regions: (1) a source-centred circle of radius 0.492 arcsec (1 pixel); and (2) an annulus of inner radius 0.492 arcsec (1 pixel) and outer radius 1.23 arcsec (2.5 pixels). The ratio of these numbers was found to be 55 $\pm$ 6. We performed a similar test with 2–5 keV events in the same regions, and found the ratio to be 19 $\pm$ 1, showing that the effect of pileup is reduced in our annular extraction region. The techniques we used to measure the core spectrum in the presence of this pileup are discussed in Section 3.2.1.

In addition to the new ACIS-S data, we made use of an earlier 40-ks ACIS-I observation taken on 2000 September 11 (ObsID 847). These data were discussed by Kerp & Mack (2003) and Sambruna et al. (2004). Because the X-ray core and inner jet were placed on the chip gaps in this observation, the data are not useful in constraining the properties of the inner regions of the source, but they provide additional information on the large-scale jet and extended emission.

Chandra images presented in this paper were made using the 0.5–5.0 keV counts in the filtered ACIS-S dataset. For the analysis of extended emission, we fitted radial surface-brightness profiles with models convolved with the *Chandra* point spread function (PSF), and extracted physical parameters (Birkinshaw & Worrall 1993). In the *Chandra* analysis of the core, the centroids of all circular and annular extraction regions were determined using the ZHTOOLS software (A. Vikhlinin, private communication).

2.2 XMM-Newton

The *XMM-Newton* observation of NGC 6251 (Gliozzi et al. 2004; Sambruna et al. 2004) was extracted from the archive for comparison with the *Chandra* datasets, and in particular to study the emission from the group environment and the large-scale jet. The data were reprocessed using the latest software and calibration files available from the *XMM-Newton* project, SAS version 6.0.0. The total exposure time was 49.3 ks (MOS1), 49.4 ks (MOS2), and 41.1 ks (pn).

To examine any periods of high background, we extracted high-energy light curves for the MOS1, MOS2, and pn cameras, in the energy range 10–12 keV (MOS) and 12–14 keV (pn), using the entire field of view in each case. The data were filtered to include events with the PATTERN=0 and FLAG=#XMMEA_EM (MOS) and #XMMEA_EP (pn) attributes only. For a more direct comparison with the method of Gliozzi et al. (2004), we extracted low-energy light curves for each camera in the energy range 0.4–10 keV, using only the CCD upon which the source was located [CCD_ID=1 (MOS); CCD_ID=4 (pn)], but excluding a circle of radius 35 arcsec centred on the source. PATTERN $\leq$ 12 (MOS) and $\leq$ 4 (pn), together with FLAG=0 attributes were selected. Inspection of both the high-energy and low-energy light curves (see Fig. 1) revealed several periods of high background, which we shall discuss further in Section 3.2.1. We also note from Figure 1 that there is little difference between the location and amplitudes of the

flares extracted using the high- and low-energy light curve methods.

The *XMM-Newton* observation of the nucleus does not suffer from significant pileup. The count rates for a source-centred circular extraction region of radius 35 arcsec were found for each of the MOS1, MOS2, and pn cameras, and are given in Table 1, together with the nominal count rates at which pileup is expected to become important. In addition, we followed the prescription of Molendi & Sembay (2003) to produce an image of diagonal bipixels in the MOS cameras (assigned PATTERN numbers 26–29), which are produced almost solely by the pile-up of two single-pixel events. No such events were found.

Spectral analysis on the large-scale jet and extended emission regions was performed using scripts based on the SAS EVSELECT tool to extract spectra from all three cameras. We included the vignetting correction by using the SAS task EVIGWEIGHT, and therefore used on-axis response files created using the SAS tasks RMFGEN and ARFGEN (for a detailed description of this method see Arnaud et al. 2002). For the jet regions, we used local background subtraction in order to remove thermal emission from the surrounding hot gas. For the extended emission, however, it was necessary to use a double subtraction technique (e.g. Arnaud et al. 2002) both for spectral analysis and for the radial surface brightness profiling used to study the spatial distribution of the emission. The double subtraction technique first takes account of the high level of particle background (which the vignetting corrections incorrectly weights up at large off-axis angles) by subtracting the counts from identical regions of a background template file, scaled to account for any differences in the particle background level of the source and background datasets. For this step, we used the background template files of Read & Ponman (2003) appropriate for each instrument and filter, with the vignetting correction applied in the same way as for the source events lists. The second step of the process accounts for the residual background by subtracting a local background taken from an outer region free of source emission. This step is necessary first because the level of X-ray background events may be different in the source and background datasets, as a result of different levels of Galactic absorption and cosmic variance, and also because the scaling required to correctly remove the particle background introduces an arbitrary scaling factor into the other components of the background that must be taken into account. For further details of the technique, see Arnaud et al. (2002), and for more discussion of our background analysis methods for *XMM-Newton* data, see Croston et al. (2003).

The radial surface brightness profiles (obtained separately for each *XMM-Newton* camera) were analysed by fitting point-source-only models and convolved point-source plus β-models to determine the significance of the contribution from extended emission. We modelled the *XMM-Newton* PSF using the most recent CCF (Current Calibration File) components: files XRT1_PSF_0007.CCF, XRT2_PSF_0007.CCF and XRT3_PSF_0006.CCF, described in the document CAL-SRN-0167-1-1, available from the *XMM-Newton* website[1].

Images were produced from the *XMM-Newton* data using the techniques described in Croston et al. (2003) to interpolate over the chip gaps and remove contaminating background point sources (identified using the *Chandra*/ACIS-I data and an adaptively smoothed image of the *XMM-Newton* data for larger radii). The image was not vignetting corrected, as the effect of incorrectly weighting up particle events at large radii would dominate over any real emission. This means that structure at larger radii is revealed in our image, but that its surface brightness is underestimated. The resulting image was smoothed using Gaussian kernels to show the distribution of extended emission, and also adaptively smoothed to show compact structure in the regions of extended emission.

2.3 Radio

The X-ray and radio structures were compared using a number of radio datasets. The best low-resolution image available was the map provided by the 3CRR Atlas[2], a 327-MHz Westerbork Synthesis Radio Telescope (WSRT) image first published by Mack et al. (1997b). This image has a resolution (FWHM of restoring circular Gaussian) of 55 arcsec. On smaller scales, we used a variety of NRAO Very Large Array (VLA) datasets, including the 1.4-GHz map of Werner (2002), 330-MHz maps taken for other purposes by one of us (Birkinshaw et al., in preparation) and datasets at 1.4, 1.6 and 8.4 GHz taken from the VLA archive, including the data used to make the images presented by Jones et al. (1986) and Jones & Wehrle (1994). A full list of the VLA datasets used and their properties is given in Table 2. Where we obtained VLA data from the archive we reduced them in the standard manner within AIPS, calibrating the flux with respect to a standard source, usually 3C 286. Maps made by others were reduced in a similar way. We combined the 1.6-GHz data of Jones et al. (1986) and Jones & Wehrle (1994), which are the most sensitive datasets available to us, subtracting from the A-configuration dataset to account for the effects of core variability, to obtain a combined dataset with sensitivity and resolution somewhat higher than that of the early maps of Perley, Bridle, & Willis (1984). This dataset is used in several of the images shown in this paper. In addition, high-resolution VLBI maps were made available to us (D. Jones, private communication). We discuss these in Section 3.2.2.

3 RESULTS

3.1 Overview of X-ray properties of NGC 6251

Figures 2 and 3 show the X-ray emission from NGC 6251 detected with *Chandra*/ACIS-S and *XMM-Newton*, respectively, with radio contours overlaid. We divide the X-rays from NGC 6251 into emission from the nucleus (Section 3.2), emission from the jet (Section 3.3), and extended thermal emission (Section 3.4). The nucleus, the brightest component, is detected with both *Chandra* and *XMM-Newton*. Components of the jet are also detected with both telescopes, although our new *Chandra*/ACIS-S observation is required to give a good image of the inner 15 arcsec of the jet. Extended thermal X-ray emission is observed on the galaxy scale with *Chandra*/ACIS-I and ACIS-S (Fig. 2), and on the group scale with *Chandra*/ACIS-I and *XMM-Newton* (Fig. 3) (see Section 3.4).

3.2 Core

3.2.1 Spectrum

a) *Chandra*

The *Chandra*/ACIS-S spectral fitting was performed over an energy range 0.5–7 keV. We chose the lower bound of the energy

---

range to be 0.5 keV, because of the known degradation of the ACIS quantum efficiency energies below ~ 0.4–0.5 keV (Marshall et al. 2004). Owing to the pileup known to be present, we tried several methods to extract and model the core spectrum. The first approach was to extract the spectrum using a source-centred circular extraction region of radius 1.23 arcsec (2.5 pixels), and to model the effect of the strong pileup known to be present using the method of Davis (2001) as implemented in SHERPA.

The second approach was to follow Gambill et al. (2003) and reduce complications due to pileup by extracting the spectrum using an annulus surrounding the source, sampling the wings of the PSF and excluding the most heavily piled-up region. The inner radius of the annulus was chosen to be 0.492 arcsec (1 pixel), which encloses $\sim$60 per cent of the core flux. We chose the outer radius to be 1.23 arcsec (2.5 pixels), which encloses $\sim$ 90–95 per cent of the core flux. The corresponding point-like ARFs (ancillary response files) were corrected for the energy-dependent missing flux using software (M. Tsujimoto, private communication) that calculates the encircled energy fraction in an annular extraction region of a model PSF created using ChaRT and MARX. This theoretical PSF was smoothed by 0.35 arcsec to take into account the broadening of the PSF associated with aspect and pixelization. Our spectral fits using this method were consistent with those in which the ARF was simply scaled by the fraction of the PSF missing in the annulus (i.e., when the energy dependence was not taken into account). Since pileup could still affect the spectrum of the annulus, we compared the results of modelling the spectrum both with and without implementing the pileup method of Davis (2001).

We compare both methods here. The spectral parameters obtained from the 2.5-pixel circle using the pileup-model [$\Gamma = 1.83 \pm 0.06$, normalization $= (1.49 \pm 0.04) \times 10^{-3}$] method were inconsistent with those from the annulus method [$\Gamma = 1.61 \pm 0.03$, normalization $= (0.87 \pm 0.02) \times 10^{-3}$]. When the effect of the moderate pileup present in the annulus was taken into account with the Davis (2001) method, the spectral parameters [$\Gamma = 1.72 \pm 0.04$, normalization $= (0.97 \pm 0.03) \times 10^{-3}$] were consistent to within $\sim 10\%$ of those obtained when the effect of the pileup was not considered, but still inconsistent with the results obtained from the circular extraction region.

We decided to investigate this discrepancy further by extracting and modelling a spectrum from the frame transfer streak, following the method of Marshall et al. (2005) to simply correct for the fraction of source events that occurred in the frame transfer streak. We found the best-fitting photon index, $\Gamma = 1.63^{+0.31}_{-0.28}$ and the normalization to be $(9.31 \pm 1.90) \times 10^{-4}$. These spectral parameters are consistent with those found using the annulus method, but again are inconsistent with those found using the circle method. We therefore adopted the annulus method for our spectral analysis, and attribute the discrepancy between the circle and annulus methods to difficulties with the pileup model in handling data sets with large pileup fractions. We note in passing that using the annulus method has the advantage of being able to model spectrally galaxy-scale thermal emission.

With an off-source background extraction region that matched the region used for radial profiling (see Section 3.4) there were 9,433 net 0.5–7 keV counts in the source-centred annulus. We grouped the data to 50 counts per PHA bin. We initially attempted to model the spectrum with a single, absorbed power-law. The fit was acceptable, but the intrinsic absorption column was poorly constrained ($N_{\rm H} \sim 8 \times 10^{18}$ atoms cm^{-2} with a 90 per cent confidence upper limit $\sim 3 \times 10^{20}$ atoms cm^{-2}). This was consistent with the value measured from 21 cm radio observations [$N_{\rm H} =$

$(4.5^{+2.6}_{-2.4}) \times 10^{20}$ atoms cm^{-2}, Werner (2002)]. We therefore decided to fix the absorbing column at its radio-measured value and performed all subsequent spectral fits using this intrinsic absorption. An absorbed power law with a photon index $\Gamma = 1.72 \pm 0.04$ gave an acceptable fit ($\chi^2 = 121$ for 136 degrees of freedom (dof)). We found a significant improvement in the fit with the addition of a thermal component in the form of a collisionally-ionized plasma model (APEC in XSPEC), with a temperature $kT = 0.20 \pm 0.08$ keV, and the abundance fixed at 0.35 solar. This model gave a good fit to the data: $\chi^2 = 107$ for 134 dof, with the probability of achieving a larger F by chance $\ll 0.1$ per cent. The spectrally measured number of 0.5–5 keV counts in the thermal component between 0.492 and 1.23 arcsec is 99 ± 28 (± 46), in agreement with the number of counts found with the radial profiling analysis (see Section 3.4), where uncertainties are quoted as 1σ (unbracketed) and 90 per cent (bracketed), for one interesting parameter. This fit is shown in Figure 4, and the best-fitting spectral parameters given in Table 3.

We confirmed the presence of the thermal emission seen by Gliozzi et al. (2004) using *XMM-Newton* data by extracting a spectrum using an annular extraction region of inner radius 0.492 arcsec and outer radius 35 arcsec (the same as used by Gliozzi et al. 2004), excluding contaminating emission from the jet and frame transfer streak. There were 11,319 net counts in the source extraction region. The best-fitting parameters of the absorbed power-law model are consistent with those found using the annulus of inner radius 0.492 arcsec and outer radius 1.23 arcsec, and the temperature of the thermal component on this scale ($kT = 0.59 \pm 0.05$ keV) is consistent with that quoted by Gliozzi et al. (2004). The measured number of counts in the thermal component between 0.492 and 35 arcsec is 912 ± 132 (± 185), with uncertainties quoted as above. This number agrees, within the errors, with the number of thermal counts found in the radial profile analysis.

We searched for the broad 6.4-keV Fe Kα emission line reported by Gliozzi et al. (2004) in the spectrum extracted from the annulus with inner radius 0.492 arcsec and outer radius 1.23 arcsec. An absorbed power law was fitted to the data over an energy range of 2.0–6.0 keV and 6.7–7.0 keV, and the interpolated continuum subtracted from the data in the energy range 6.0–6.7 keV. The continuum parameters were consistent with those found previously, and provided a good fit to the data ($\chi^2 = 8.34$ for 6 dof in the energy range 5.5–7.0 keV). A Gaussian Fe emission line, with a centroid allowed to vary between 6.2 and 6.7 keV, and free line width was then added to the model. The line energy was poorly constrained, and the decrease in the fit statistic ($\Delta\chi^2 = 6.18$ for three additional parameters) not significant on an F-test (the probability of a larger F by chance is 21 per cent). As an additional test, the data were regrouped to 5 counts per PHA bin and the Cash-statistic used to evaluate the goodness of fit. Again, the line energy was poorly constrained, and the decrease in fit statistic ($\Delta C = 9.14$) small.

Further, a Gaussian Fe Kα emission line, with best-fitting parameters matching those found with *XMM-Newton* (Gliozzi et al. 2004), was added to the *Chandra* continuum model. The *XMM-Newton*-measured emission line gave a decrease in the fit statistic of $\Delta\chi^2 = 3.14$ for three additional parameters that was not significant (the probability of a larger F by chance is 65 per cent). Finally, the line parameters were changed to match those detected with *ASCA* (Turner et al. (1997). Again, the decrease in the fit statistic was not significant ($\Delta\chi^2 = 2.79$ for three additional parameters). However, we note that the non-detection of Fe Kα emission with *Chandra* is unsurprising, given the relatively low

effective area of the ACIS camera at 6.4 keV.

b) *XMM-Newton*

A goal of our *XMM-Newton* analysis was to make an independent evaluation of the fluorescent Fe Kα emission from the nucleus claimed by Gliozzi et al. (2004). As mentioned in Section 2, the *XMM-Newton* observation of NGC 6251 is severely contaminated by background flares. Contamination from background flares is a serious concern in the analysis of the low surface-brightness jet and extended emission regions, whereas for the high signal-to-noise core spectra it is less important. However, it is still important to assess carefully the effect of the background flares on the nuclear spectral analysis.

To achieve this, we adopted several good time interval (GTI)-filtering criteria based upon both the high-energy and low-energy light curves discussed in Section 2.2 and presented in Figure 1. The criteria we used are described below, and the effective exposure and number of 4–10 and 5.5–7.5 keV counts within a 35 arcsec source-centred circle are shown in Table 4 for each GTI filtering method.

(i) Conservative filtering based on 10–12 keV (MOS) and 12–14 keV (pn) light curves. The maximum allowed count rates were 0.25 s^{-1} (MOS) and 1 s^{-1} (pn)

(ii) 3σ filtering based on 10–12 keV (MOS) and 12–14 keV (pn) light curves. Good time intervals were created by excluding data after 44.6 ks (MOS) and 42.6 ks (pn) (corresponding to the last flare), and calculating the time periods when the remaining data are within $\pm 3\sigma$ of the mean level.

(iii) 3σ filtering based on 0.4–10 keV light curves (MOS and pn). As above.

The *XMM-Newton* spectral fitting was performed jointly for the MOS1, MOS2 and pn cameras for an energy range of 0.4–10 keV, using each of the GTI-filtering methods described above. We extracted source spectra using a circular extraction region of radius 35 arcsec centred on the source. Background spectra were extracted using a source-centred annular extraction region of inner radius 140 arcsec and outer radius 280 arcsec for the MOS cameras, and an off-source rectangle for the pn camera. Only events with FLAG=0 and PATTERN $\leq$ 12 (MOS) and $\leq$ 4 (pn) were included in our analysis. The data were grouped to 40 counts per PHA bin.

As a representative example, we describe the fitting to the continuum performed on the data filtered using the 3σ method based on the high-energy light curves data: the spectral parameters derived using the other GTI-filtering methods are entirely consistent with this case. We initially attempted to model the spectrum with a single, absorbed power-law, with the intrinsic absorption was fixed at 4.5×10^{20} atoms cm^{-2}. The normalizations of all spectral components were kept free for each camera. For completeness, and following Gliozzi et al. (2004), an Fe Kα emission line at ~ 6.4 keV was modelled with a Gaussian function and is discussed later. The fit was poor: $\chi^2 = 1347$ for 1135 dof. However, a substantial improvement in the fit was obtained by adding a thermal component with a temperature $kT = 0.60 \pm 0.07$ keV, and abundance fixed at 0.35 solar. The new fit was acceptable ($\chi^2 = 1197$ for 1131 dof), with the probability of achieving a larger F by chance $\ll 0.1$ per cent. The counts spectrum and best-fitting model, together with contributions to χ^2 is shown in Figure 5. The best-fitting spectral parameters for the *XMM-Newton* observation are given in Table 3.

We also used the *XMM-Newton* data to search for possible fluorescent line emission from iron, and considered the statistical significance of its detection for each GTI-filtering method described above. An absorbed power law was fitted to the spectrum over an energy range of 2.0–5.0 keV and 7.5–10.0 keV, and the interpolated continuum subtracted from the data in the energy range 5.0–7.5 keV. The continuum parameters were consistent with those described above, and provided a good fit to the data. The energy range was then extended to cover 5.0–7.5 keV, and the continuum parameters frozen. A Gaussian Fe emission line with a centroid allowed to vary between 6.0 and 6.9 keV and free line width was then added to the model, and the significance of its addition assessed with an F-test. This spectral analysis was performed for the MOS1+MOS2 cameras jointly, the pn camera only, and finally all three jointly. A summary of the significances is given in Table 5, the best-fitting parameters are shown in Table 6, and counts spectra for the pn camera are presented in Figure 6.

Our results show that a continuum-only model provides an adequate fit to the spectra, and that any Fe Kα detection is entative, but not highly significant, even when an unconservative GTI-filtering method is used. Figure 6, in particular, illustrates that different methods of extracting light curves for GTI filtering purposes, i.e., using high-energy or low-energy light curves, has no effect on our conclusions. We also note that the only evidence for the existence of the Fe Kα line is in the data from the pn camera; however, this is perhaps not surprising, as the effective area of the pn camera is still somewhat higher than that of the MOS1+MOS2 cameras combined.

For a more direct comparison with the results of Gliozzi et al. (2004), we chose to investigate further the properties of the Fe Kα line measured in the spectrum of the pn camera. We chose the 3σ-filtering criterion based on the low-energy (0.4–10 keV) light curves described in Section 2.2, which most closely matches the GTI-filtering method used by Gliozzi et al. (2004). We created confidence contours of the line energy and line width, as shown in Figure 7. This test shows that the line parameters are very poorly constrained. Even when the line width was frozen at 0.4 keV and the fitting reperformed, the confidence contours of the line energy and normalization (Fig. 7) show that the line parameters are still highly uncertain.

3.2.2 Source variability

a) X-ray

For the *XMM-Newton* data, we attempted to confirm the intra-observation variability claimed by Gliozzi et al. (2004) by creating X-ray light curves for each of the MOS1, MOS2, and pn cameras, using a source-centred circular extraction region of radius 35 arcsec. Background subtraction was applied using a source-centred annular extraction region of inner radius 140 arcsec and outer radius 280 arcsec for the MOS cameras, and an off-source rectangle for the pn camera. Only events with FLAG=0, PATTERN $\leq$ 4 (MOS) and $\leq$ 12 (pn), and an energy 0.8–10 keV were included in our analysis. In this instance, the good time intervals were chosen to be the same as those used by Gliozzi et al. (2004).

The *XMM-Newton* data were binned to a variety of timescales, and a χ^2 analysis used to test the null hypothesis. Statistically significant variability was only found with a long bin time. With bins of 3 ks, we found that the variability found in the data from the pn camera was significant ($\chi^2 = 22.35$ for 13 dof; null hypothesis probability = 95.0 per cent). Further, a co-added light curve for all three cameras was produced and binned to 3 ks. We found the variability to be significant ($\chi^2 = 26.07$ for 12 dof; null hypothesis probability = 99.0 per cent). We do, however, caution that times corresponding to periods of high background are present in

this light curve. While the background level is significantly lower than the source count rate, we cannot be certain of its impact on the extracted light curves. Background-subtracted results for the individual *XMM-Newton* cameras, as well as the sum of their data, are given in Table 7.

For the *Chandra* data, we attempted to search for variability on 3-ks timescales by extracting an ACIS-S light curve from a source-centred circle of radius 1.23 arcsec, with an off-source background extraction region that matched the choice of background for the radial profiling (see Section 3.4). Unlike the *XMM-Newton* observations, no significant variability was found on 3-ks timescales ($\chi^2 = 13.37$ for 16 dof), although this might be due to the limited sensitivity of *Chandra* compared with *XMM-Newton*. We note that fitting a line of gradient of 8.31×10^{-4} cts s^{-2} to the data is significantly preferred ($\Delta\chi^2 = 7.77$ for one additional parameter) over a uniform source brightness. Background-subtracted results for *Chandra* are given in Table 7. Finally, we constructed a light curve of the hardness ratio, $H - S/H + S$, where S is the 0.7–1.5 keV count rate and H the 3–7 keV count rate, binned to 3 ks. The variability of the hardness ratio was not significant ($\chi^2 = 13.62$ for 16 dof).

Finally, in Table 8, we tabulate the long-term 2–10 keV power-law luminosity and photon-index history of NGC 6251. The 2–10 keV power law luminosity has varied by a factor of $\sim$5 during 1991–2003, while not all of the photon-index values are mutually consistent. The *Chandra* photon index of 1.67 ± 0.06 is somewhat flatter than that measured with *XMM-Newton*, but it is entirely plausible that variability has occurred.

b) Radio

High-resolution VLBI observations of NGC 6251 (e.g., Jones et al. 1986) show a compact, self-absorbed core with a highly inverted spectrum and a parsec-scale jet. Emission from the core does not greatly dominate over that from the jet in the VLBI observations, even at the highest available frequency of 10.7 GHz, where it is most prominent. We used VLBI observations of NGC 6251 (D. Jones, private communication) to estimate the flux densities of the core and jet at several epochs and frequencies. The results are given in Table 9. This shows that variability approaching a factor of 2 has occurred on timescales of years.

c) Optical

Hubble Space Telescope (*HST*) images of the central regions of NGC 6251 have shown an unresolved optical core, surrounded by a dusty disk (Ferrarese & Ford 1999). Optical core flux densities were measured by Hardcastle & Worrall (1999) and Chiaberge et al. (2003) from archival *HST* observations. There now exist *HST* data from several epochs that we can use to search for any optical and UV variability. We performed photometry on multi-epoch data from the WFPC2 instrument (F555W and F814W filters) and from the FOC instrument (F342W and F410M filters). Following Hardcastle & Worrall (1999), the source flux was determined using a circular extraction region of radius 5 pixels (0.2 arcsec), using background from an annular region of inner radius 5 pixels and outer radius 10 pixels. As noted by Chiaberge et al. (2003), the largest source of systematic error in determining the flux from the WFPC2 data is the choice of background, as a result of the dusty disk surrounding the nucleus. Unresolved nuclear emission in the FOC data dominates by a large factor over extended emission, so the systematic errors may not be as high. The measured count rates were converted to flux densities at the central fre-

quency of each filter, using the SYNPHOT photometry package and assuming a power law with $\alpha = 0.8$.

The reddening to NGC 6251 is the sum of Galactic and possibly intrinsic components. The Galactic value was calculated using a standard relationship between the neutral hydrogen column density and the $B - V$ colour excess (Burstein & Heiles 1978). We estimated the Galactic $B - V$ colour excess to be 0.061 mag, in fair agreement with the value calculated using the dust maps of Schlegel, Finkbeiner, & Davis (1998) (0.087 mag). To convert between the $B - V$ colour excess and the extinction, we used the extinction curve of Schild (1977). As an example, this gives rise to a B-band extinction, $A_B = 0.25$ mag. In addition, *if* the hydrogen column that obscures the radio core (Werner 2002) also covers the optical core, we estimate a *further* extinction by assuming the same extinction ratio as our Galaxy.

The measured core flux densities for the multi-epoch *HST* data are tabulated in Table 10, assuming both Galactic and intrinsic absorption. This shows that the flux densities measured with the WFPC2 instrument have varied by < 10 per cent over a period of ~ 1 year. However, data from the FOC instrument are separated by ~ 5 years, and show variability by a factor ~ 3.

3.3 Jet

X-ray emission from the jet of NGC 6251 comes from three regions: the 'inner jet', extending from about 1.5 arcsec to 27 arcsec from the nucleus, which corresponds to the *ROSAT* HRI detection of Hardcastle & Worrall (1999); and two regions of the outer jet, which we call regions 1 and 2, corresponding to 'knots' 1 and 2 of Kerp & Mack (2003), and extending respectively between about 200–265 arcsec and 330–410 arcsec from the core. The new *Chandra*/ACIS-S observation clearly detects the inner jet and region 1 (Fig. 2), but region 2 falls off the CCD. The *Chandra*/ACIS-I data give a detection of all three regions (Fig. 1 of Kerp & Mack 2003), though the inner jet is only weakly detected because of the positioning of core and jet in the area of the central chip gap. Between the end of the inner jet and the start of region 1, (i.e., between 30 and 200 arcsec from the core) there is a $3-4\sigma$ excess of counts over the local background in the ACIS-S data (about 50 0.5–5 keV counts), suggesting that there is some X-ray emission associated with this region of the radio jet (the 'middle jet'). The data are not sensitive enough to allow us to associate this detection with a particular component of the radio emission. In the *XMM-Newton* data both components of the outer jet (region 1, discussed by Sambruna et al. 2004, and region 2) are detected, although the spatial resolution of *XMM-Newton* means that the inner jet is confused with the core. For the *XMM-Newton* analysis of the jet and extended emission, we used the 'conservative' GTI filtered data described in Section 3.2.1b.

The relationship between the radio jet and the inner X-ray jet is shown in Figure 8. The inner jet, which contains 380 ± 20 0.4–7.0 keV *Chandra*/ACIS-S counts, appears similar to the radio emission; for example, a bright knot ('a') at 5 arcsec from the nucleus is present in both radio and X-ray images, while there is a dip in both radio and X-ray surface brightness at around 9 arcsec ('b'). At around 15 arcsec from the nucleus ('c'), the X-ray jet brightens while the surface brightness of the radio jet drops, and there are hints that the X-ray jet, which is transversely resolved with *Chandra*, may be edge-brightened at this point; thereafter the flux in X-rays drops off rapidly with distance along the jet (Fig. 9). A spectral fit to the whole jet region, using an adjacent background of the same shape and at the same distance from the nucleus, is well fitted

($\chi^2 = 7.6$ for 15 dof) with a single power-law model absorbed with the Galactic column density; the photon index is $2.29^{+0.14}_{-0.13}$ (1σ for one interesting parameter) and the 1-keV flux density of this region of the jet is 10 ± 1 nJy. A thermal (MEKAL) model with moderate (0.3 solar) abundance is a much worse fit, with $\chi^2 = 28.5$ for 15 dof. There is no evidence for differences in the power-law index as a function of position in the jet; if we divide it into inner and outer halves containing approximately equal numbers of counts, the fitted power-law indices for the two halves are 2.6 ± 0.3 and 2.2 ± 0.3 respectively.

The two outer regions of the X-ray jet correspond to brighter features in the low-frequency radio image, and the X-ray structure of region 1, at least, is well matched to the radio (Fig. 2). There is no sign of knotty or compact structure in either the radio or X-ray; the compact feature appearing at about 230 arcsec from the nucleus in Figure 5 of Jones & Wehrle (1994) does not appear in our reduction of their VLA dataset, and we suspect it to have been an imaging artefact. We extracted spectra for region 1 from the two *Chandra* datasets, using rectangular regions with adjacent off-source background, and also from the three *XMM-Newton* cameras, using a similar but somewhat broader region to account for the larger *XMM-Newton* PSF. A fit to the ACIS-S dataset alone gives a good fit to a power-law model with Galactic absorption and photon index $1.96^{+0.23}_{-0.21}$, but a joint fit to all five datasets in the 0.4–7 keV energy range gives a good fit ($\chi^2 = 30.4$ for 26 dof) with lower, though consistent, power-law index (1.68 ± 0.13) and a 1-keV flux density of 4.7 ± 0.4 nJy. We tested the significance of the detection for region 2 by comparing source and background counts for the three *XMM-Newton* cameras. We measured 205 background-subtracted 0.4–7.0 keV counts in the source region, and 1686 counts in the background (when scaled to the size of the source region), giving a $> 3\sigma$ level detection (the detection is also significant for each separate camera). The best-fitting power-law spectrum ($\chi^2 = 8.2$ for 7 dof) fitted to the three *XMM-Newton* cameras in region 2, again using a rectangular extraction region, has a photon index of $1.7^{+0.8}_{-0.7}$, with a 1-keV flux density of $3.4^{+1.0}_{-1.1}$ nJy. In both these cases the data can be fitted equally well with thermal models with moderate abundance, but high temperatures are required (5 keV in the case of region 1, even higher in region 2).

3.4 Extended emission

To search for any extended emission on 10–100 kpc scales, a radial profile was extracted using data from the *Chandra*/ACIS S3 chip in the energy range 0.5–5.0 keV. The profile was centred on the nucleus, and excluded one detected background point source, as well as jet emission, which was excluded by ignoring a pie slice between the position angles 284 and 302 degrees. The radial profile extended from 0.98 arcsec (2 pixels) out to 84 arcsec (170 pixels), with background taken from an annulus of inner radius 84 arcsec and outer radius 118 arcsec (240 pixels) (see Figure 10). A PSF was modelled using ChaRT and MARX, and was convolved with a Gaussian of r.m.s. width 0.35 arcsec in order to provide a good match with the radial profile data close to the core.

The radial profile analysis gave an unacceptable fit to single-component models of either a point source or a β-model (used to describe gas in hydrostatic equilibrium), but a combination of the two gave an acceptable fit ($\chi^2_\nu = 0.79$), as shown in Figure 11. The best-fitting parameters of the β-model were $\beta = 0.595^{+0.065}_{-0.045}$ and $\theta_c = 2.527^{+1.393}_{-1.251}$ (all errors are 1σ for two interesting parameters, i.e., $\chi^2_{\min} + 2.3$). The FWHM of the gas distribution is ~ 2 kpc, which is comparable to that seen in other radio-loud ellipti-

cals, such as 3C 31 (1.7 kpc, Hardcastle et al. 2002a). In our annular spectral extraction regions of radii 0.492 – 1.23 arcsec and 0.492 – 35 arcsec (see Section 3.2.1), we would expect to see 94^{+123}_{-39} ($^{+220}_{-49}$) and 1499 ± 315 (± 494) thermal counts respectively, where uncertainties are quoted as 1σ (unbracketed) and 90 per cent (bracketed), for two interesting parameters.

The extended emission on larger scales, previously discussed by Birkinshaw & Worrall (1993), Mack, Kerp, & Klein (1997a) and Sambruna et al. (2004), is clearly seen in our maps of the *XMM-Newton* data (Fig. 3). The emission is roughly radially symmetric and centred on the radio source, though there is an X-ray deficit to the SW of the nucleus (also seen by Mack, Kerp, & Klein 1997a) that does not appear to be related to any of the radio structure. To characterize this emission, we extracted radial profiles for the three *XMM-Newton* cameras and for the *Chandra*/ACIS-I data. The profiles were obtained in the energy range of 0.3–7 keV out to a radius of 450 arcsec; the inner 2 arcsec of the *Chandra* profile was excluded to avoid the chip gaps. We fitted single point-source models and convolved point-source plus β-models to the *XMM-Newton* profiles. For all profiles, the point-source models were not an adequate fit to the data, so that the inclusion of the β-model component is needed. In all cases, the inclusion of a β-model of suitable parameters leads to good values for the fit statistic (an improvement from $\chi^2 = 132$ for 43 dof to $\chi^2 = 47.9$ for 42 dof for MOS1, from $\chi^2 = 111$ for 46 dof to $\chi^2 = 46.7$ for 45 dof for MOS2, and from $\chi^2 = 677$ for 28 dof to $\chi^2 = 26.5$ for 27 dof for pn). We tested the significance of the improvement separately for each camera using Monte Carlo simulations (as in Croston et al. 2004), and in each case we found a probability of < 0.1 per cent that the improvement in χ^2 given above could occur by chance. Figure 12 shows the pn profile with a point-source model and the best-fitting point-source plus β-model. For the ACIS-I dataset, we included a fixed small-scale β-model based on the ACIS-S data in the fit, and were then able to obtain adequate fits with an additional large-scale β-model component. We find the best-fitting parameters for a joint fit to the ACIS-I, MOS1, MOS2 and pn profiles to be $\beta = 0.90^{+0.6}_{-0.25}$, $r_c = 116^{+64}_{-38}$ arcsec (errors are 1σ for 2 interesting parameters), which are consistent with the best-fitting models found by Birkinshaw & Worrall (1993) for the *ROSAT* data. The individual datasets all give best-fitting parameters that are consistent at the joint 1σ level. The joint fit is good ($\chi^2 = 152$ for 134 degrees of freedom). The residuals are dominated by systematic uncertainties in the modelling of the *XMM-Newton* PSF and in the background subtraction at large radii.

We extracted spectra from the three *XMM-Newton* cameras to study the extended emission identified by the radial profile analysis, using the 'conservative' GTI-filtering described in Section 3.2.1b. We used an extraction annulus between 60 and 300 arcsec and used the double subtraction technique described in Section 2.2 to obtain appropriate background spectra. The radial profile analysis shows that there is a significant contribution from the bright central point source at these radii. We included this contribution in the spectral fits as a fixed component with the parameters of our best-fitting core spectrum (an *apec* model of $kT = 0.60$ keV and $Z = 0.35$ solar, and a power-law with $\Gamma = 1.85$), scaling the normalizations by the fraction of encircled energy in the extraction region (8.3 per cent). In addition to this fixed component, we fitted a second APEC model for the extended emission. We found a best-fitting temperature of $1.7^{+0.4}_{-0.3}$ keV and abundance of $0.4^{+0.4}_{-0.2}$ solar (both consistent with the results of Sambruna et al. 2004), with χ^2 of 292 for 305 degrees of freedom.

For all three *XMM-Newton* cameras, the total counts in the

β model between radii of 60 and 300 arcsec are consistent with the counts in the thermal component of the best-fitting spectrum described above. The total bolometric luminosity for the group atmosphere, determined by integrating the β-model, is found to be $(7 \pm 1) \times 10^{41}$ ergs s^{-1}.

4 INTERPRETATION

4.1 Core

The nuclear continuum spectrum of NGC 6251 detected with *Chandra* and *XMM-Newton* is well described by an absorbed power-law model. This result is consistent with two distinct models for the nuclear X-ray emission from radio galaxies. The first is that the non-thermal X-radiation is dominated by emission from an accretion flow, via inverse-Compton upscattering of a population of lower-energy photons to X-ray energies. Such a model would be supported by the detection of broadened fluorescent Fe Kα emission of high equivalent width. However, our analysis of the *XMM-Newton* observation first presented by Gliozzi et al. (2004) has shown that the detection of the Fe Kα line is not *highly* significant (a continuum-only model provides an adequate fit to the spectrum), leading us to disfavour such a model. The line is not detected with *Chandra*, although this is possibly related to the relatively poor photon statistics of the ACIS camera at 6.4 keV. Further, the poorly constrained parameters using the *XMM-Newton* data mean that it is impossible to constrain its origin, much less to argue that it originates in the inner regions of an accretion disk.

A second possible interpretation of the data (Birkinshaw & Worrall 1993; Chiaberge et al. 2003) is that the X-ray emission arises primarily from the subparsec radio VLBI jet. To investigate this model further, we calculated the flux density ratio of the 1-keV power-law X-ray emission measured with *Chandra* and the parsec-scale radio jet seen in 5-GHz VLBI observations (Jones et al. 1986). We performed a similar calculation for the inner (kiloparsec-scale) jet, using our *Chandra*/ACIS-S observation and 8-GHz VLA observations. As shown in in Table 11, the slopes and flux-density ratios of the X-ray and radio components of the parsec- and kiloparsec-scale emissions are approximately similar. This similarity also occurs with the nearby radio galaxy Centaurus A, where the soft nuclear X-ray component is interpreted as having a jet origin (Evans et al. 2004). The similar observed variability on timescales of years of the radio, optical, and X-ray data might also suggest a common origin for the nuclear emission, although we note that the data are non-contemporaneous, so no firm conclusions can be drawn.

Previous studies of the X-ray and radio flux properties of the active nuclei of low-power radio galaxies (Fabbiano et al. 1984; Worrall & Birkinshaw 1994; Canosa et al. 1999; Hardcastle & Worrall 1999) have shown a correlation between the luminosities of soft, unresolved X-ray emission and 5-GHz core radio emission. NGC 6251 lies near the trendline established for the large B2 sample of radio galaxy cores (Canosa et al. 1999). This is consistent with the hypothesis that the observed X-ray emission is associated with the parsec-scale VLBI jet. This is not the only possible interpretation. For example, Merloni, Heinz, & Di Matteo (2003) find evidence for a correlation between the X-ray and radio luminosities, together with the black hole mass, of a sample of 100 AGN, and relate the X-ray emission to an accretion flow. However, the majority of their target objects are not radio galaxies, and so may not possess relativistic parsec-scale jets.

In order to place further constraints on the X-ray emission mechanism, we constructed a spectral energy distribution of the nucleus of NGC 6251, using observations from VLBI (D. Jones, private communication), ISO (Birkinshaw et al., in preparation), *HST* (present work; Hardcastle & Worrall 2000; Chiaberge et al. 2003), *Chandra* (present work), *XMM-Newton* (present work), *BeppoSAX* (Guainazzi et al. 2003), *ASCA* (Turner et al. 1997), *ROSAT* (Birkinshaw & Worrall 1993), and *CGRO*/EGRET (Mukherjee et al. 2002). *HST* data were dereddened following the method described in the preceding section. The SED is double-peaked, and is similar to previously-determined SEDs for NGC 6251 (e.g., Chiaberge et al. 2003), where the authors argued that the SED is consistent with a blazar-type model, with the X-rays being produced by synchrotron-self Compton (SSC) emission. Figure 13 shows a plausible SSC model fit to the radio-to-X-ray emission of NGC 6251, which has been more extensively discussed elsewhere (Chiaberge et al. 2003; Guainazzi et al. 2003; Ghisellini, Tavecchio, & Chiaberge 2004).

It is possible, however, that in this jet-dominated scenario there exists a 'hidden' accretion-related component of luminosity of the order 10^{41} ergs s^{-1}. Such a model would permit a fluorescent Fe Kα line, and indeed for NGC 6251 we speculate that the (weak) detection of the line is evidence for this model. We shall return to this point elsewhere (Evans et al., in preparation). It is further possible that the relative strength of jet- and accretion-related components varies over time: as noted by Guainazzi et al. (2003), states of high nuclear luminosity might correspond to periods when emission from a relativistic jet dominates the observed X-ray flux, whereas during lower-luminosity periods, emission from an accretion flow might be most prominent. This is supported by the fact that the most significant detection of a fluorescent Fe Kα line, with ASCA in 1994 (Turner et al. 1997; Guainazzi et al. 2003), occurred when the continuum flux was at its lowest historical level (see Table 8).

4.2 Jet

The natural interpretation of the inner jet is as a synchrotron jet similar to those seen in other FRI-type radio galaxies (e.g. Hardcastle, Birkinshaw, & Worrall 2001). The steep X-ray spectrum is hard to reconcile with any other emission mechanism and, as seen in Table 12, the X-ray-to-radio flux ratio is similar to those seen in the resolved jets of other low-power radio galaxies where the jet emission is interpreted as synchrotron in nature. Additional support for this model comes from the detection of an apparent optical counterpart of the jet (Werner 2002). The optical jet is detected between about 8 and 20 arcsec from the nucleus, and a simple synchrotron model with a broken power-law electron energy spectrum can be fitted to the radio, optical and X-ray data in this region without difficulty, with the low-frequency spectral index α being 0.5 and the high-frequency value 1.1 (Fig. 14). This model is similar to those fitted to other radio, optical and X-ray jets.

For an equipartition magnetic field strength in this region (around 2 nT) the electron energy-loss timescale for an X-ray-emitting electron is of the order of a few hundred years, while the light travel time to the base of this region is $\sim 1.2 \times 10^4$ years, ignoring the effects of projection and beaming (which may be considerable, as we discuss below). The synchrotron origin of the X-ray emission from the inner jet requires *in situ* particle acceleration in this source. [Kerp & Mack (2003) come to a different conclusion, but their calculation of the loss timescale is based on a magnetic field strength which is inappropriate for the inner jet.] *In situ* parti-

cle acceleration in turn requires an energy source. In the case of the well-studied FRI jets in 3C 31 it has been argued (Hardcastle et al. 2002a; Laing & Bridle 2004) that the energy for the particle acceleration that produces the observed X-ray jet comes from the bulk deceleration of the jet flow, a process that plausibly happens for many other FRI jet sources in which the jet-counterjet asymmetry decreases with distance from the nucleus (e.g., Laing et al. 1999). If we believe that the jet-counterjet asymmetry in the case of NGC 6251 (whose one-sided radio jet is morphologically very similar to those seen in other FRI sources) is due to relativistic beaming, then clearly the jet does not decelerate to sub-relativistic speeds in the inner few kiloparsecs, as other well-studied FRI jets in sources of similar luminosity apparently do, but instead retains at least moderately relativistic speeds out to hundreds of kpc. However, based on the radio sidedness evidence alone, we cannot rule out a model in which some deceleration occurs in the inner 13 kpc (projected) in which we see the inner X-ray jet, and in which the deceleration provides the energy source for the required particle acceleration.

The interpretation of the outer jet is less obvious. In region 1, the synchrotron model that we fitted to the inner jet significantly overpredicts the X-ray flux density; more importantly, the best-fitting spectral index is too flat. The two-point spectral index between 1.4 GHz and 1 keV is 0.95, while the best-fitting X-ray spectral index is 0.71, which taken at face value rules out a one-zone synchrotron model (the low-frequency radio spectral index is ~ 0.5). Spectral indices as steep as 1.09 are not ruled out at the 99 per cent confidence level, so we can devise a one-zone synchrotron model in which the electron energy spectrum breaks immediately after the radio region to a spectral index ~ 1 and then continues to the X-ray. We do not regard this model as impossible, but it involves ad hoc assumptions about the electron energy spectrum and is only marginally consistent with the X-ray data. Region 1 is much larger than the synchrotron loss scale for X-ray emission electrons in an equipartition magnetic field strength, so we have no particular reason to expect a one-zone synchrotron model to be applicable, but nevertheless it is clear that region 1 is not well described by the sort of model that has traditionally been fitted to the inner synchrotron jets of FRIs, including NGC 6251.

Ignoring thermal models (which cannot explain the close relationship between radio and X-ray emission) the alternative simple model for region 1 is the one favoured by Sambruna et al. (2004), in which the jet is highly relativistic and the X-ray emission is caused by scattering of the boosted microwave background radiation (e.g., Tavecchio et al. 2000). This model naturally explains the flat spectral index, which would be expected to be similar to the low-frequency radio index (0.5–0.6). Such models have been used to describe the jets in core-dominated Fanaroff-Riley type II (FRII) quasars, but in general in FRIs we might expect the jets to be too slow to exhibit significant effects, and the model also requires small values of the angle θ of the jet to the line of sight. In NGC 6251, however, we have already seen that the jet does not appear to decelerate to sub-relativistic speeds on 10-kpc scales, so that it is possible that the 100-kpc-scale jet could be produced by beamed inverse-Compton emission. To investigate this, we calculated the expected inverse-Compton flux density for a grid of bulk Lorentz factors and angles to the line of sight θ. We assumed a minimum electron Lorentz factor of 10 and a maximum of 4×10^5, an electron power-law index of 2 (corresponding to a spectral index α of 0.5) and Doppler boosting appropriate to a continuous jet ($S \propto \mathcal{D}^{2+\alpha}$, where $\mathcal{D}$ is the Doppler factor) and took account of the variation of the length of the jet as a function of θ. The anisotropic

nature of the inverse-Compton emission was accounted for using the code described by Hardcastle et al. (2002b), which implements the results of Brunetti (2000). The result of our calculations was a grid of Lorentz factor and angle, from which we were able to interpolate the range of allowed angles for a given Lorentz factor, given the observed X-ray flux density. The requirements for beaming parameters are quite extreme. A bulk Lorentz factor as low as ~ 2.5 ($\beta \approx 0.92$) is possible, but only if the jet is pointing almost directly along the line of sight, which is clearly not the case. For more reasonable values of θ, the required bulk Lorentz factor is larger, and the model requires $\theta < 15°$ for $\Gamma < 16$ ($\beta < 0.998$) (Fig. 15). These high bulk speeds would have to be maintained across the well-resolved X-ray jet, ~ 10 kpc in width. Whereas there is some evidence for a spine-sheath model involving relativistic speeds on parsec scales in BL Lac objects (e.g. Chiaberge et al. 2000), and the spine speeds in such models are comparable to those required to produce the observed level of X-rays through the beamed inverse-Compton process, we emphasise that, if this were to persist to Mpc scales (as required here) it would *not* produce the X-ray jet structure seen in NGC 6251 – instead, we would expect an X-ray jet that was significantly narrower than the radio region.

Other constraints on the angle to the line of sight and jet speeds come from analysis of the jet-counterjet ratio on the parsec and kiloparsec scales: for example, the lower limit on the high-frequency parsec-scale jet-counterjet ratio (R) determined by Jones & Wehrle (2002), $R > 128$, would imply $\theta < 40°$ if all the jet-counterjet asymmetry were attributed to beaming. On larger scales, a weak kiloparsec-scale counterjet is detected in some images, implying $R = 40$ (Perley, Bridle, & Willis 1984); if $\theta < 40°$, this would imply $\beta < 0.84$ on those scales. But in region 1 of the outer jet the jet-counterjet ratio is > 200, requiring either higher speeds or a change in the angle to the line of sight. All of these arguments are based on the assumption that the jet and counterjet are steady and intrinsically symmetrical, which is dangerous, since some of the properties of the large-scale jet are probably influenced by the large-scale environment, as we shall argue later. Although the one-sided parsec- and kiloparsec-scale jets provide some evidence for relativistic speeds and angles to the line of sight $\lesssim 40°$, they cannot tell us convincingly whether the constraints on the CMB boosting model (Fig. 15) are reasonable. Finally, it is worth noting that NGC 6251 is already one of the largest known radio galaxies, with a *projected* linear size close to 2 Mpc. It is therefore *a priori* unlikely that the whole source structure is close to the line of sight.

Region 2 provides few additional constraints. In this region, the simple synchrotron model fitted to the inner jet gives a good prediction of the observed 1-keV flux density (within the large errors); the weak constraints on the X-ray spectrum mean that this model is acceptable in that respect too. However, the large size of the region means that only moderate amounts of beaming are required to provide the observed X-ray in the boosted inverse-Compton model (Fig. 15). Thus, both a synchrotron and inverse-Compton model are possible without difficulty for this component. The inverse-Compton model would require a change in jet speed and/or orientation, since the constraints on beaming parameters are not consistent with those determined for region 1. But we know that the jet does bend, in projection, at around region 1, so this is not impossible. On the other hand, the weakly detected middle jet (between 30 and 200 arcsec from the core) does provide an important additional constraint. The X-ray counts in the ACIS-S data for this region correspond to a 1-keV flux density, assuming a similar spectrum to the other components, around 1.4 nJy. But the large

size of the middle jet region means that it should be a relatively good source of beamed IC. With parameters similar to those determined from region 1, we overpredict the observed X-ray emission by a factor ~ 5. The inverse-Compton model can only explain this if (a) the jet speeds up significantly between the middle jet and region 1, or (b) there is a significant change in the angle to the line of sight between the middle jet and region 1, in the sense that the jet bends towards us at region 1, with all the bending taking place perpendicular to the plane of the sky; for bulk Lorentz factors around 5–7, the flux constraints require that the middle jet have $\theta > 20°$. We regard both of these *ad hoc* assumptions as unlikely.

We conclude that all possible models for the X-ray emission for region 1 of the jet are problematic to some extent, but that a synchrotron model is more consistent with what is already known about FRI jets and with the large-scale properties of the source. This then leaves us with the question of why regions 1 and 2 are particularly good sites for X-ray synchrotron emission and the corresponding *in situ* particle acceleration. We return to the nature of these regions in the next section.

4.3   Extended emission

The detection of large and small-scale thermal components allows us to investigate the long-standing question of jet confinement in NGC 6251. We can estimate the minimum pressures in the jet components in the standard way, choosing a conservatively low minimum electron energy corresponding to $\gamma_{\min} = 10$, assuming a low-energy electron energy index of 2 (which is consistent with the observed low-frequency behaviour of the jet) and using the spectrum that fits the radio, X-ray and optical data at higher energies. We assume no significant contribution from relativistic protons, so that these are true minimum-energy values. The remaining uncertainties are projection and beaming effects. Beaming *in general* makes the jet appear brighter than it really is, and so causes us to overestimate the minimum pressure. Projection, which goes along with beaming, causes us to underestimate the true size of components, so again we overestimate their pressure: but it also means that they are further out in the thermal atmosphere than we expect.

If we assume that the source is in the plane of the sky (measured lengths are true lengths) and that there is no beaming, the results are shown in Table 13 and plotted in Fig. 16. We see that the minimum pressures are close to the external thermal pressures for all these regions, except for the lobe, where the internal minimum pressure is much lower than the external pressure, as seen in other sources. (Note however that the outer pressure for the lobe is an extrapolation of the fitted β model well beyond the region where emission is seen, so that it should be treated with caution.) As the effects of beaming will tend to reduce the pressures in the jet components, these results suggest (contrary to what was found in earlier work) that the jet can be close to pressure balance with the external medium over its entire length. We have repeated the calculations using two beaming models: firstly, one that can reproduce the sidedness in the inner kiloparsec-scale jet ($\theta = 40°$ and $\beta = 0.8$), and secondly, one that could produce the X-ray emission from region 1 on an inverse-Compton model ($\theta = 12°$, $\beta = 0.98$). For both these models, the change in the ratio of radio to thermal pressure is uniformly a decrease (though in the second case the thermal pressures at large distances are uncertain). Including the possible effects of beaming and projection thus only strengthens the conclusion that the jet is underpressured, or at best in pressure balance with the thermal emission at minimum pressure. The main differences between our analysis and that of Birkinshaw & Worrall (1993) are (1)

the additional small-scale thermal component, (2) slightly lower minimum pressures in this work [as a result of slightly more conservative assumptions than those used by Perley, Bridle, & Willis (1984)] and (3) slightly higher estimated thermal pressures in the large-scale thermal emission. We stress that our calculation assumes that the jet is electron-positron (with no heavy content) and is radiating at minimum energy.

Does the extended thermal emission tell us anything about the structure and dynamics of the radio source? We begin by noting that Fig. 3 appears to show an arm of X-ray-emitting gas at the northern edge of the radio lobe, similar to the rim of material seen around the southern lobe of 3C 449 (Hardcastle, Worrall, & Birkinshaw 1998; Croston et al. 2003). If real, this feature would indicate that the lobe is behaving similarly to other FRI radio galaxies and inflating a large-scale cavity in the X-ray gas. The FOV of *XMM-Newton* prevents us from seeing whether this feature extends to the far end of the N lobe. More interestingly, from the point of view of the overall interpretation, there is a significant drop in surface brightness, first pointed out by Kerp & Mack (2003), evident in Fig. 3 at roughly the distance of region 1 of the X-ray jet, where the radio and X-ray jets brighten and the extended lobe radio emission begins. (This drop in surface brightness is not obvious in the radial profiles of Fig. 12, but these specifically exclude emission in the direction of the jet.) If the positional agreement between the edge of the radio lobe and the drop in X-ray surface brightness is not coincidental, it implies that the radio *lobe* axis is reasonably close to the plane of the sky – if the lobe were strongly projected, it would be hard to see a discontinuity in the X-ray. This is not impossible to reconcile with the constraints on jet angle to the line of sight $\theta \lesssim 40°$, since the lobe subtends a large angle ($70°$) as seen from the nucleus, provided that the jet enters the lobe towards the surface nearer to the observer, though it is hard to reconcile with the very small angles to the line of sight required in an inverse-Compton model. If the jet X-ray emission is synchrotron, then the fact that there is relatively strong X-ray and radio emission at region 1 may be a reflection of particle acceleration at a pressure discontinuity, or at some other interaction as the jet enters the lobe. The weaker X-ray emission at region 2 could then be an interaction between the jet and the edge of the lobe, since the jet bends between region 1 and region 2, and must bend again if it is to connect with the 'warm spot' at the end of the lobe. The geometry of this model of the jet and lobe is sketched in Figure 17.

Finally, we note that, by integrating the best-fitting large-scale β-model to derive the group-scale luminosity, and using the radio-quiet L_X/T_X relation (Croston et al. 2003), we would predict a temperature of ~ 0.65 keV, which is significantly less than the measured value. This may suggest some heating of the thermally emitting gas by the radio source. As the radio lobes of this source are large, the PdV work done in expansion is expected to be considerable. We calculate, based on the external pressure at the radius of the lobes, and an assumed volume of 1.5×10^{66} m^3 (modelling the lobe as a sphere of radius 230 kpc, based on the extent of the low-frequency radio emission), that the work done by the western lobe is $\sim 3 \times 10^{52}$ J. A simple calculation of the heat capacity of the entire group, $C = (3/2)Nk$, where N is the total number of particles, calculated using the spectral and spatial parameters for the group atmosphere, shows that if the energy transferred from the radio lobes is distributed throughout the group atmosphere it would raise the temperature of the gas by ~ 0.6 keV. Therefore, if the eastern lobe also contributes a similar amount of energy (it is of similar size), then the temperature of the NGC 6251 group gas may be explained as a result of radio-source heating due to expansion of

the lobes. This is consistent with our observations of other sources (Croston et al. 2003; Croston, Hardcastle, & Birkinshaw 2005), although the uncertainties are large.

5 CONCLUSIONS

We have presented results from *Chandra*/ACIS-S and ACIS-I and *XMM-Newton*/EPIC observations of the nucleus, jet, and extended emission of the radio galaxy NGC 6251. For the nucleus, we find the following.

(i) The X-ray spectrum is well fitted by an absorbed power-law with thermal emission. There is tentative, but not highly significant, evidence for the detection of an Fe $K\alpha$ line with *XMM-Newton*.

(ii) The nuclear spectral energy distribution is double-peaked, similar to that found by Chiaberge et al. (2003), and is well-fitted with a synchrotron self-Compton model. This lends support to a model in which the nuclear X-ray emission is due to inverse-Compton upscattering of low energy photons in a relativistic jet to higher energies.

(iii) It is plausible that some of the X-ray emission originates in an accretion flow (rather than a jet), and that the relative dominance of accretion- and jet-related components varies with time.

For the kiloparsec-scale jet and extended emission, our conclusions are as follows.

(i) There is a well-detected inner X-ray jet with a broad-band spectrum and X-ray properties similar to those of other X-ray jet sources, implying local particle acceleration in the inner 10–20 kpc.

(ii) Inverse-Compton models for the previously detected large-scale jet emission ('regions 1 and 2' in our notation) require extreme parameters; coincidences in geometry are required to explain the non-detection of the inner part of the jet. Although a one-zone synchrotron model is only marginally viable for region 1, we prefer a synchrotron over an inverse-Compton explanation for both this region and region 2. In the synchrotron picture, regions 1 and 2 may be privileged sites for particle acceleration as a result of interactions between the jet and the lobe.

(iii) Kiloparsec-scale thermal emission is present in NGC 6251, with properties similar to that found in other radio-loud ellipticals, as well as the previously known group-scale thermal emission. We are able to characterize the properties of both the galaxy-scale and group-scale components and show that the pressure of the thermal gas can confine the jet if it is at minimum energy and contains no significant contribution from heavy particles, particularly if (as seems likely) relativistic beaming is important.

(iv) The detailed relationship between the northern radio lobe and the extended X-ray emission suggests that the radio lobe has evacuated a cavity in the X-ray-emitting gas, as seen in other FRI sources. If so, the sharpness of the boundary between gas and lobe suggests that the lobe is close to the plane of the sky, and that the jet enters the lobe close to the surface nearer the observer.

(v) The group gas is somewhat hotter than expected for its luminosity, and the work done in expanding the radio lobes provides a plausible source for the additional heat.

6 ACKNOWLEDGEMENTS

References

Arnaud M., et al., 2002, A&A, 390, 27
Birkinshaw, M., Worrall, D. M., 1993, ApJ, 412, 568
Brunetti G., 2000, Astroparticle Physics, 13, 107
Burstein D., Heiles C., 1978, ApJ, 225, 40
Canosa C. M., Worrall D. M., Hardcastle M. J., Birkinshaw M., 1999, MNRAS, 310, 30
Chiaberge M., Celotti A., Capetti A., Ghisellini G. 2000, A&A, 358, 104
Chiaberge, M., Gilli, R., Capetti, A., Macchetto, F. D. 2003, ApJ, 597, 166
Cohen, M. H., Readhead, A. C. S. 1979, ApJ, 233, L101
Croston J. H., Hardcastle M. J., Birkinshaw M., Worrall D. M., 2003, MNRAS, 346, 1041
Croston J. H., Birkinshaw M., Hardcastle M. J., Worrall D. M., 2004, MNRAS, 353, 879
Croston J. H., Hardcastle M. J., Birkinshaw M., 2005, MNRAS, 357, 279
Davis, J. E. 2001, ApJ, 562, 575
Evans D. A., Kraft R. P., Worrall D. M., Hardcastle M. J., Jones C., Forman W. R., Murray S. S., 2004, ApJ, 612, 786
Fabbiano, G., Trinchieri, G., Elvis, M., Miller, L., Longair, M. 1984, ApJ, 277, 115
Ferrarese, L., Ford, H. C. 1999, ApJ, 515, 583
Foschini L., et al., 2004, A&A accepted, preprint (astro-ph/0412285)
Gambill, J. K., Sambruna, R. M., Chartas, G., Cheung, C. C., Maraschi, L., Tavecchio, F., Urry, C. M., Pesce, J. E. 2003, A&A, 401, 505
Ghisellini, G., Tavecchio, F., Chiaberge, M. 2004, A&A accepted, preprint (astro-ph/0406093)
Ghizzardi, S. 2001, "In-flight calibration of the PSF for the PN camera", XMM-SOC-CAL-TN-0023, available from http://www.xmm.vilspa.esa.es
Gliozzi, M., Sambruna, R. M., Brant, W. N., Mushotzky, R., Eracleous, M. 2004, A&A, 413, 139
Guainazzi, M., Grandi, P., Comastri, A., Matt, G. 2003, A&A, 410, 131
Hardcastle M. J., Worrall D. M., Birkinshaw M., 1998, MNRAS, 296, 1098
Hardcastle, M. J., Worrall, D. M. 1999, MNRAS, 309, 969
Hardcastle M. J., Worrall D. M., 2000, MNRAS, 314, 359
Hardcastle M. J., Birkinshaw M., Worrall D. M., 2001, MNRAS, 326, 1499
Hardcastle M. J., Birkinshaw M., Cameron R. A., Harris D. E., Looney L. W., Worrall D. M., 2002, ApJ, 581, 948
Hardcastle, M. J., Worrall, D. M., Birkinshaw, M., Laing, R. A., Bridle, A. H. 2002, MNRAS, 334, 182
Hardcastle M. J., Worrall D. M., Kraft R. P., Forman W. R., Jones C., Murray S. S., 2003, ApJ, 593, 169
Hardcastle, M. J., Worrall, D. M., Birkinshaw, M., Laing,

R. A., Bridle, A. H. 2005, MNRAS, accepted, preprint (astro-ph/0412599)

Ho L. C., 1999, ApJ, 516, 672

Jones, D. L., et al. 1986, ApJ, 305, 684

Jones D. L., Wehrle A. E., 1994, ApJ, 427, 221

Jones, D. L., Wehrle, A. E. 2002, ApJ, 580, 114

Kerp, J., Mack, K.-H. 2003, New Astronomy Review, 47, 447

Laing R. A., Parma P., de Ruiter H. R., Fanti R., 1999, MNRAS, 306, 513

Laing R. A., Bridle A. H., 2004, MNRAS, 348, 1459

Mack K.-H., Kerp J., Klein U., 1997, A&A, 324, 870

Mack K.-H., Klein U., O'Dea C. P., Willis A. G., 1997, A&AS, 123, 423

Marshall, H. L., Tennant, A., Grant, C. E., Hitchcock, A. P., O'Dell, S. L., Plucinsky, P. P. 2004, SPIE, 5165, 497

Marshall, H. L., *et al.* 2005, ApJS 156, 13

Merloni A., Heinz S., Di Matteo T. 2003, MNRAS, 345, 1057

Molendi, S., Sembay, S. 2003, "Assessing the EPIC Spectral Calibration in the Hard Band with a 3C273 Observation", XMM-SOC-CAL-TN-0036, available from http://www.xmm.vilspa.esa.es

Mukherjee, R., Halpern, J., Mirabal, N., Gotthelf, E. V. 2002, ApJ, 574, 693

Murphy, E. M., Lockman, F. J., Laor, A., Elvis, M. 1996, ApJS, 105, 369

Perley R. A., Bridle A. H., Willis A. G., 1984, ApJS, 54, 291

Protassov, R., van Dyk, D. A., Connors, A., Kashyap, V. L., Siemiginowska, A. 2002, ApJ, 571, 545

Read A. M., Ponman T. J., 2003, A&A, 409, 395

Sambruna, R. M., Gliozzi, M., Donato, D., Tavecchio, F., Cheung, C. C., Mushotzky, R. F. 2004, A&A, 414, 885

Schild R. E., 1977, AJ, 82, 337

Schlegel D. J., Finkbeiner D. P., Davis M., 1998, ApJ, 500, 525

Shuder J. M., Osterbrock D. E., 1981, ApJ, 250, 55

Sudou, H., Taniguchi, Y., Ohyama, Y., Kameno, S., Sawada-Satoh, S., Inoue, M., Kaburaki, O., Sasao, T. 2000, PASJ, 52, 989

Tavecchio F., Maraschi L., Sambruna R. M., Urry C. M., 2000, ApJ, 544, L23

Turner, T. J., George, I. M., Nandra, K., Mushotzky, R. F. 1997, ApJS, 113, 23

Waggett P. C., Warner P. J., Baldwin J. E., 1977, MNRAS, 181, 465

Wilson, A. S., Yang, Y. 2002, ApJ, 568, 133

Werner, P. N., Ph.D. thesis, Univ. Bristol

Worrall, D. M., Birkinshaw, M. 1994, Ap.J., 427, 134

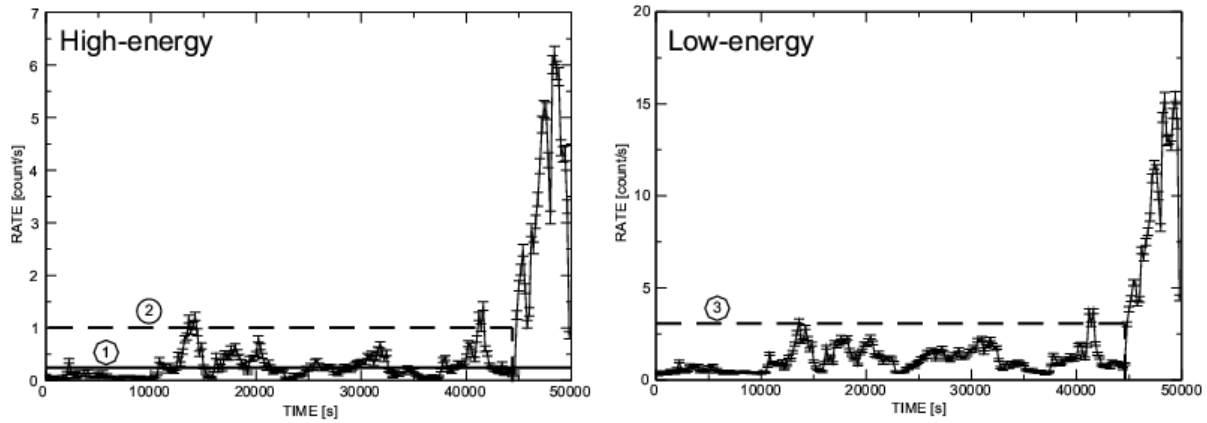Worrall D. M., Birkinshaw M., Hardcastle M. J., 2003, MNRAS, 343, L73

Figure 1. *XMM-Newton* MOS1 light curves used to evaluate good-time intervals. Left: High-energy (10-12 keV) light curve for the whole field of view. Right: Low-energy (0.4–10 keV) light curve for CCD 1, excluding the source. Also shown are the time/count rate filtering criteria in the conservative case (1) and the 3σ filtering case (2 and 3), as defined in Section 3.2.
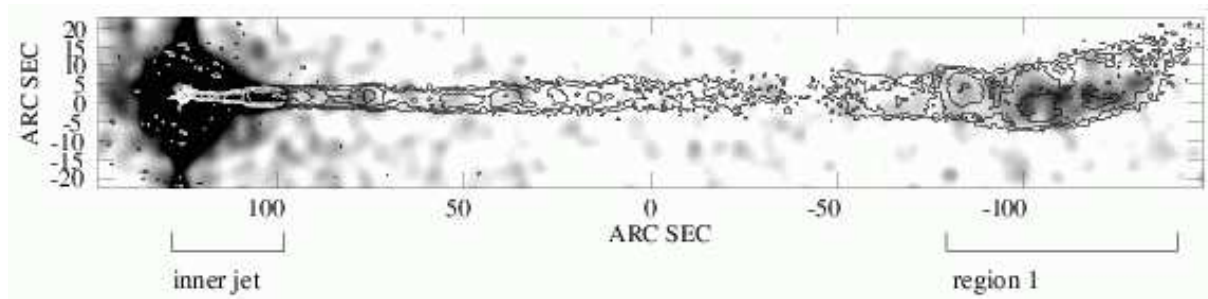

Figure 2. The inner jet and region 1 of the outer jet (as defined in the text) of NGC 6251 as seen in the new *Chandra*/ACIS-S data. The image is smoothed with a 4-arcsec FWHM circular Gaussian; superposed are contours of the 1.6-GHz radio map discussed in Section 2.3 at $0.2 \times (1, 2, 4 \dots)$ mJy beam^{-1}. The image shown here has been rotated through -24.4 degrees.
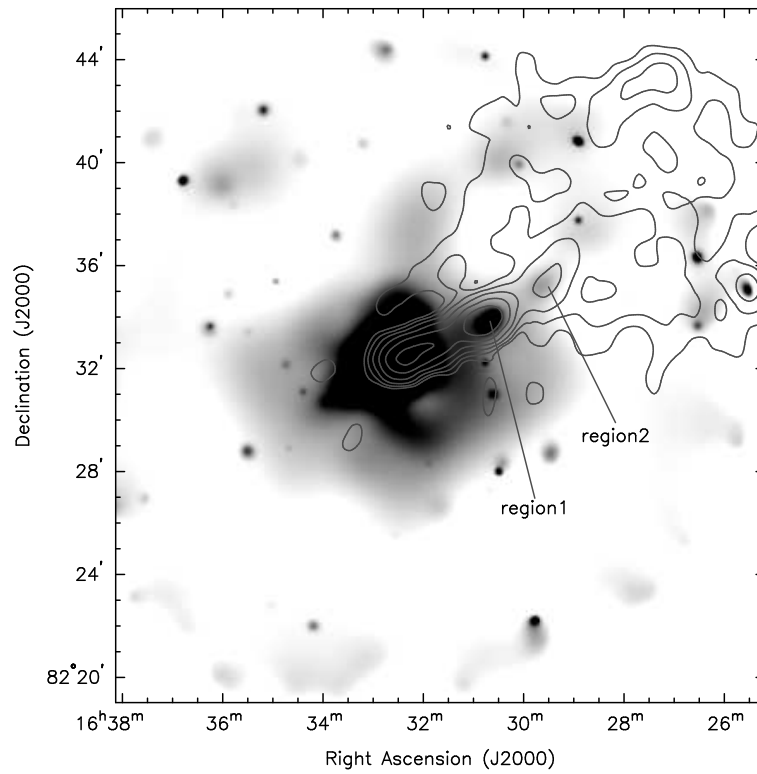
Figure 3. Adaptively smoothed, combined MOS1, MOS2 and pn image in the 0.5–5 keV energy band, with radio contours overlaid. The image shows the relation between the X-ray and radio jet and large-scale extended emission. Radio contours are from the Westerbork 327-MHz map discussed in Section 2.3. Contour levels are 1,2,4...16 $\times 2 \times 10^{-2}$ Jy beam^{-1}. The radio/X-ray source on the W edge of the image is presumably a background AGN, though no optical counterpart is detected in DSS images.
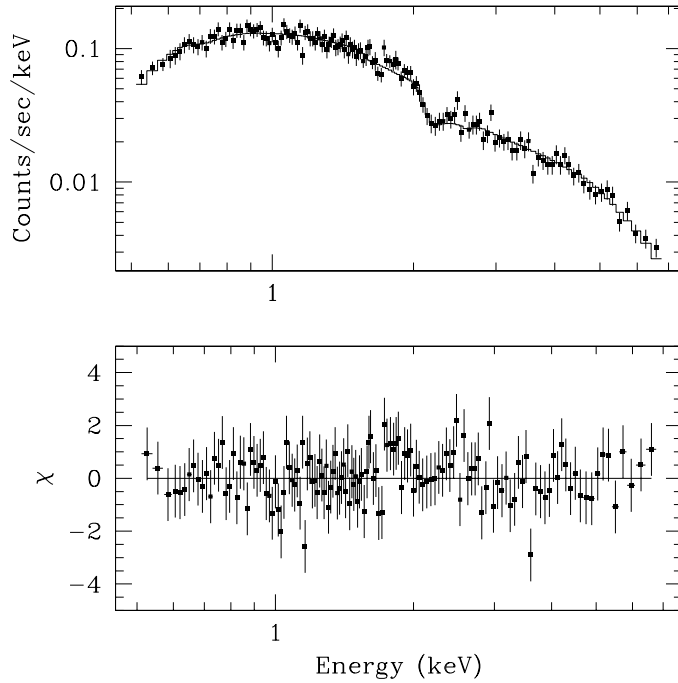
Figure 4. Spectral fit to data from the *Chandra* observation in the energy range 0.5–7 keV with a power-law and APEC model, with the abundance fixed at 0.35 solar. The spectral extraction region was a source-centred annulus of inner radius 0.492 arcsec and outer radius 1.23 arcsec. Contributions to χ^2 are also shown.
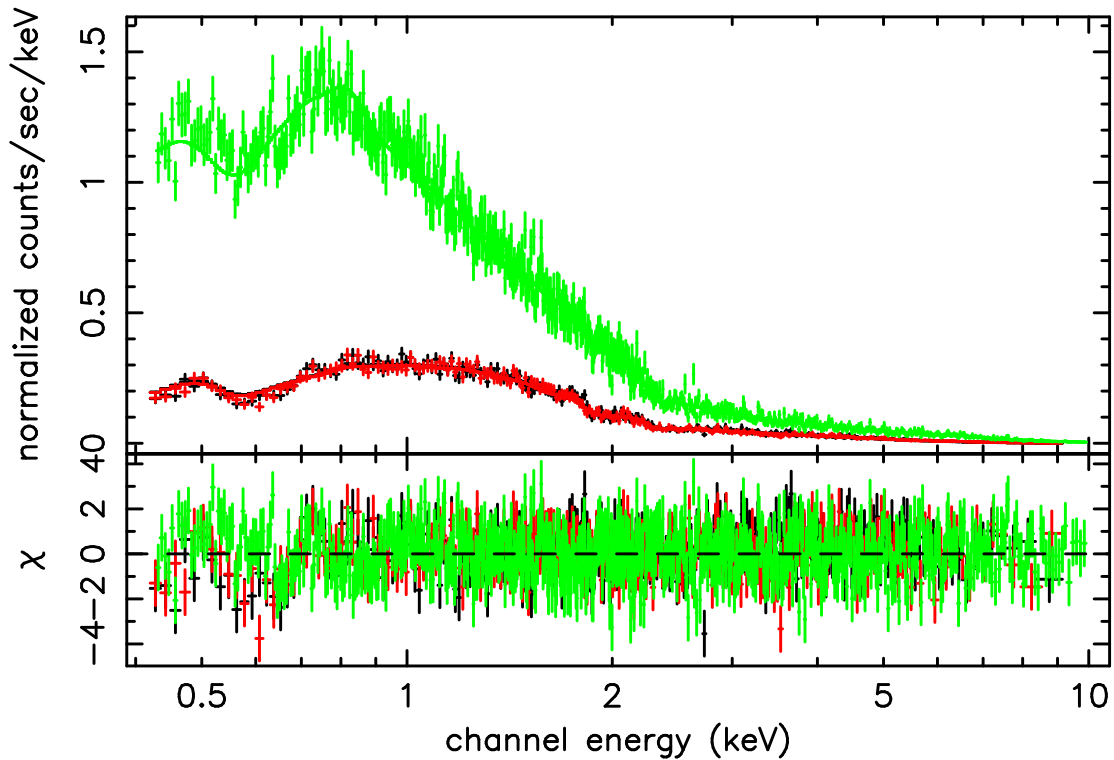

Figure 5. Spectral fit to data from the *XMM-Newton* observation in the energy range 0.4–10 keV with a power-law and APEC model, with the abundance fixed at 0.35 solar. A Gaussian line was included in the fit for completeness. Contributions to χ^2 are shown. The GTI filtering was performed using the 3σ method defined in Section 3.2; the continuum parameters found when using the other GTI-filtering methods are consistent with this case.
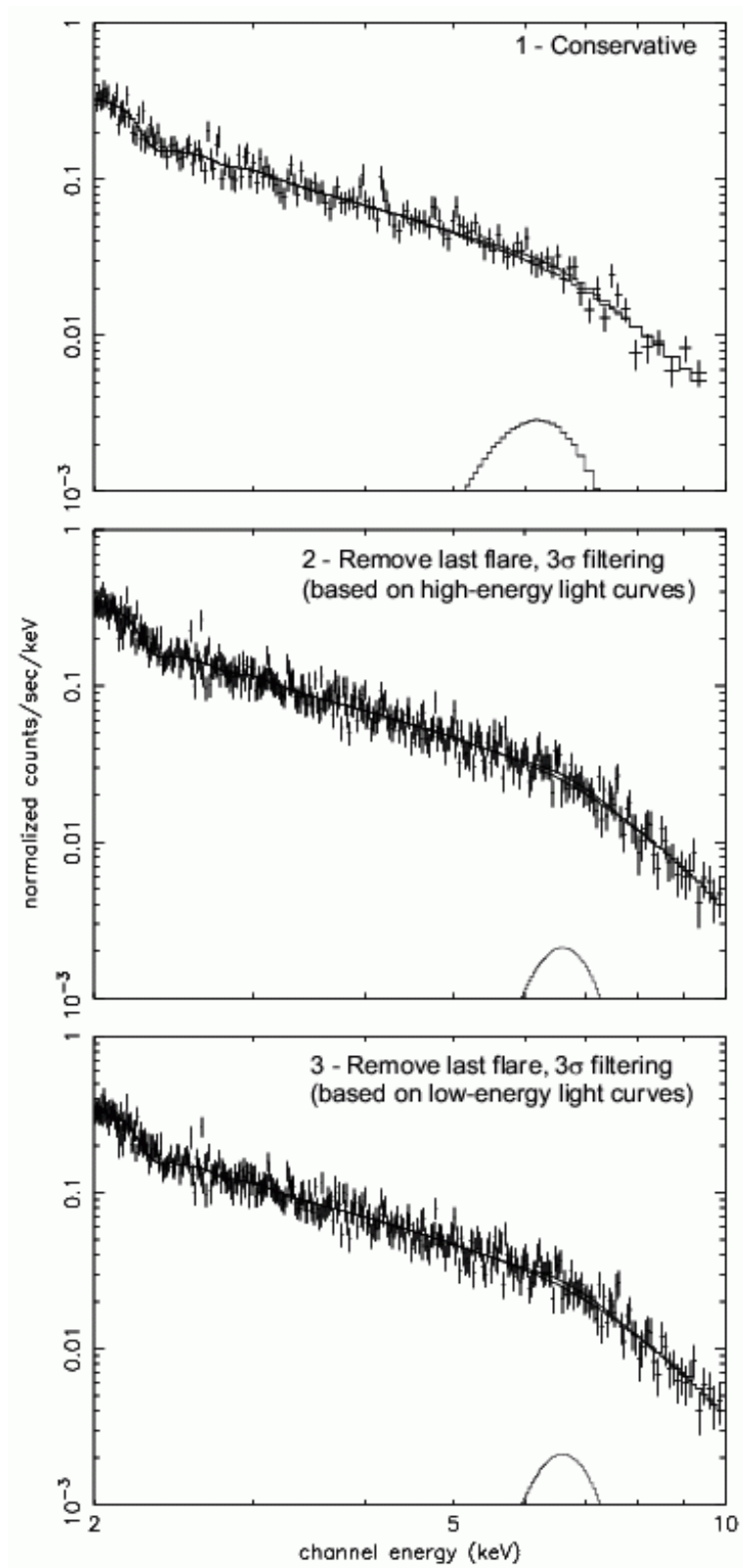
Figure 6. Counts spectra for the pn camera, showing the model contributions from an absorbed power law, a Gaussian emission line, and their sum. Shown are the three GTI filtering methods used for the *XMM-Newton* nuclear spectral analysis, as defined in Section 3.2.
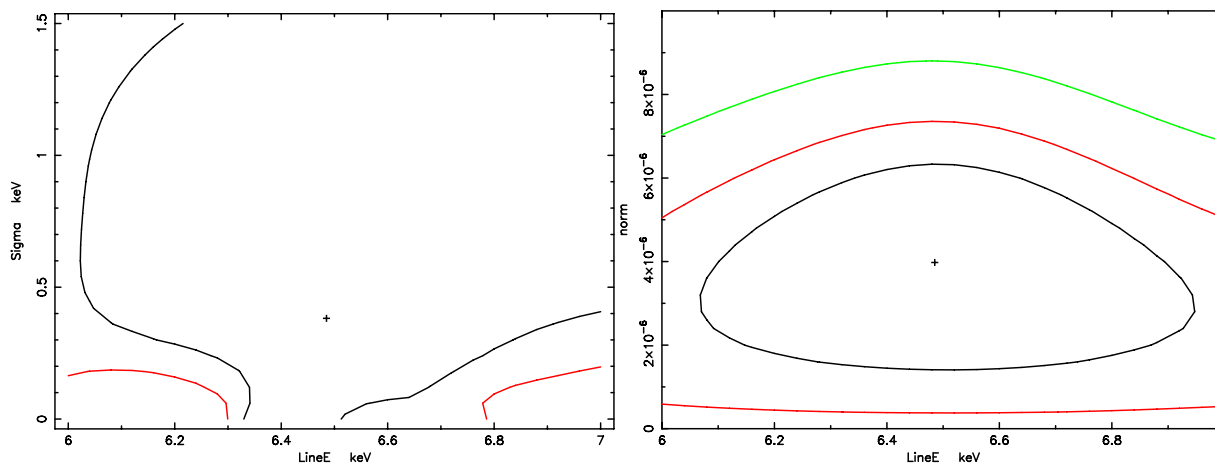
Figure 7. Left: Energy and line width confidence contours of the Fe Kα line for the pn spectrum using the 3σ GTI-filtering method based on the low-energy light curve. Right: Energy and normalization confidence contours of the Fe Kα line, after freezing the line width at 0.4 keV and reperforming the spectral fitting. This highlights the poor constraints that can be placed on the Fe Kα line-parameters, even though an unconservative GTI-filtering method was used.
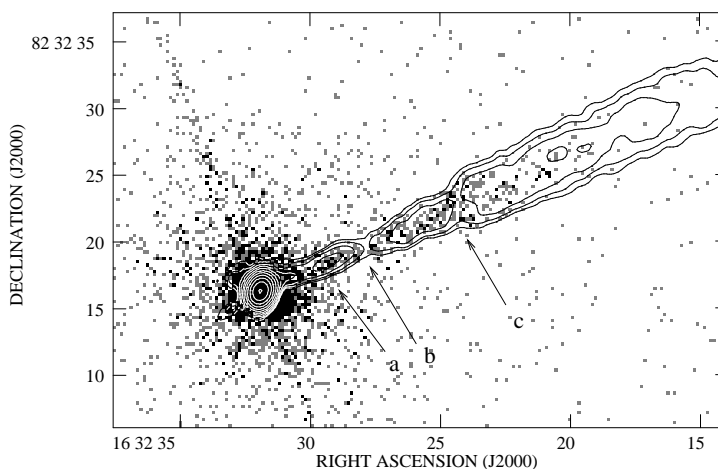
Figure 8. The inner jet of NGC 6251. The greyscale shows *Chandra* X-ray counts between 0.5 and 5 keV, binned in 0.246-arcsec pixels; black is 2 counts pixel^{-1}. Superposed are contours from a radio map made from the A- and B-configuration VLA data at 1.6 GHz, with a resolution of 1.36×1.09 arcsec, at $(1, 2, 4 \dots) \times 0.4$ mJy beam^{-1}. The arrows show (a) a bright knot at 5 arcsec from the nucleus visible in both radio and X-ray, (b) a dip in the surface brightness at both wavebands, and (c) a bright region of the X-ray jet coincident with a dip in the radio surface brightness at 15 arcsec from the nucleus.
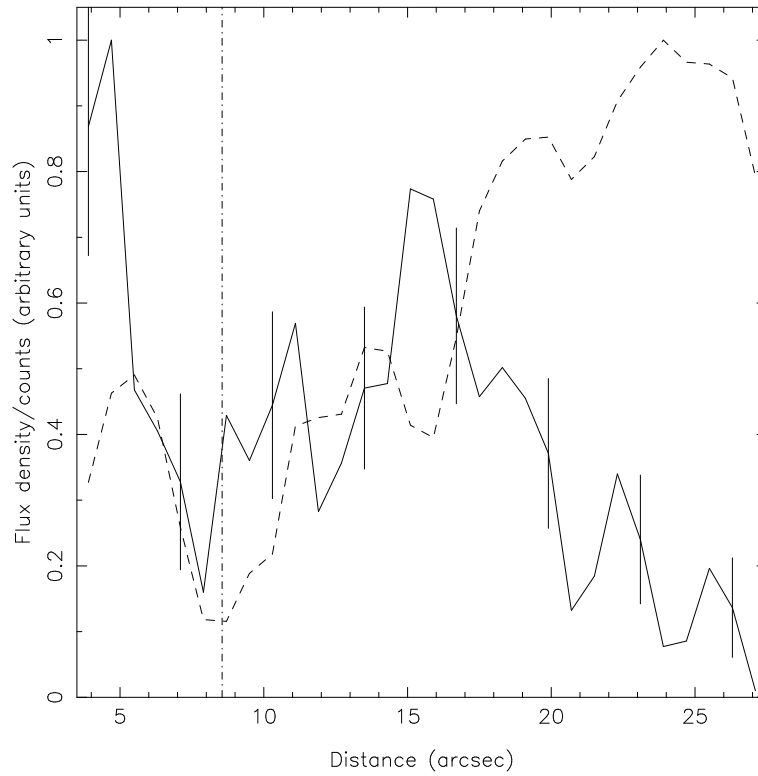
Figure 9. A profile along the inner jet of 6251 in radio (dashed line) and X-ray (solid line). Data are taken from a rectangular strip 5.7 arcsec wide, with adjacent background subtraction in the case of the X-ray data, and binned in 0.8-arcsec bins. The vertical dot-dashed line shows the position of the dip in the radio surface brightness ('b' on Fig. 8). The vertical lines on the X-ray points indicate the Poisson errors.
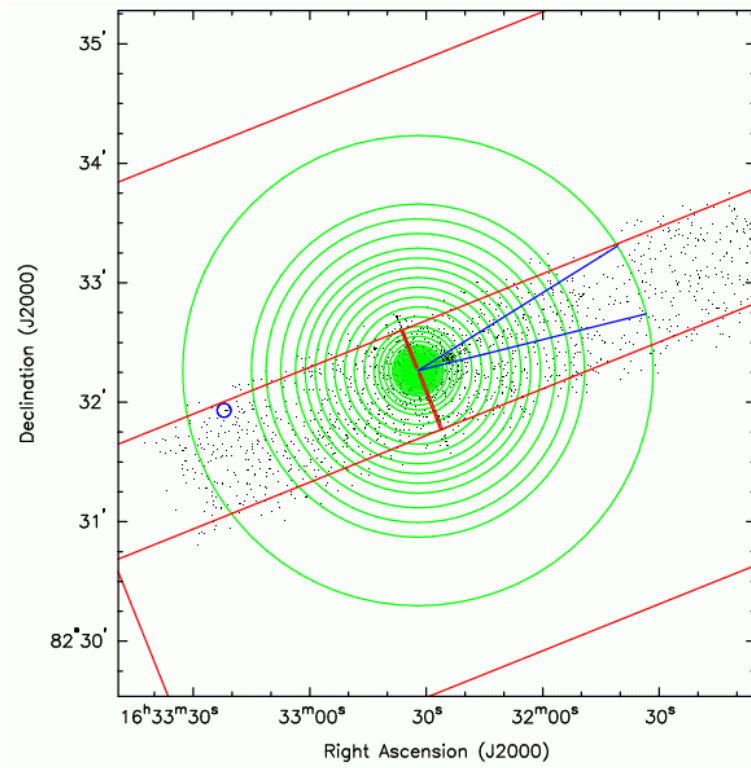
Figure 10. Regions used in the *Chandra*/ACIS-S radial profiling analysis. Concentric circles of radii 0.98–118 arcsec (2–240 pixels) are shown. Background was extracted from the last annulus (170–240 pixels). The regions excluded from the analysis were the two large outer rectangles, the two small rectangles (masking the frame transfer streak), a small circle (masking a point source), and a pie slice between position angles 284 and 302 degrees (avoiding contamination from jet emission).
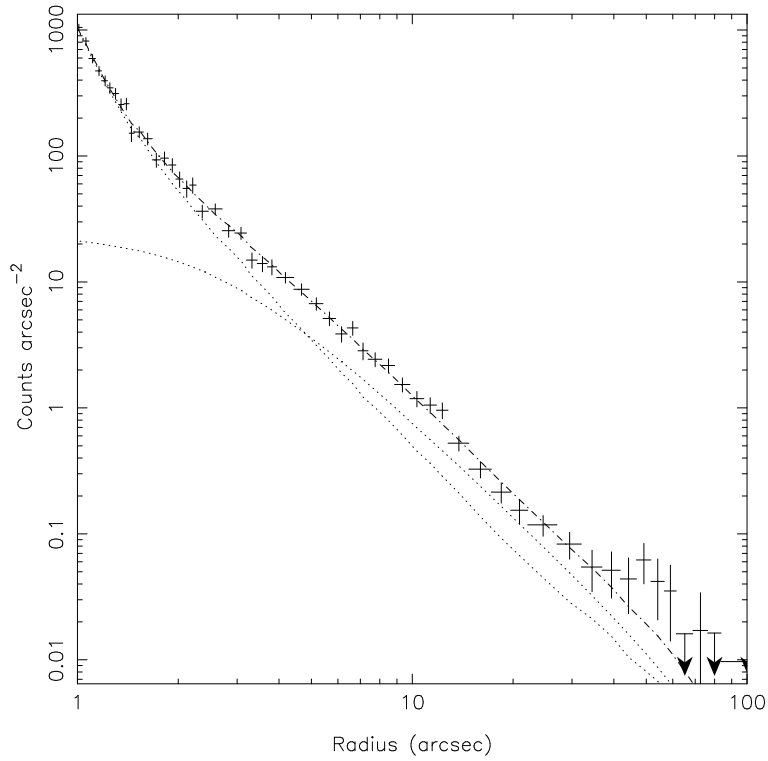
Figure 11. Background-subtracted 0.5–5 keV radial surface brightness profile for the *Chandra*/ACIS-S data. The best-fitting model is a composite of a point-like component and a β-model, with the best-fitting β-model parameters described in the text.
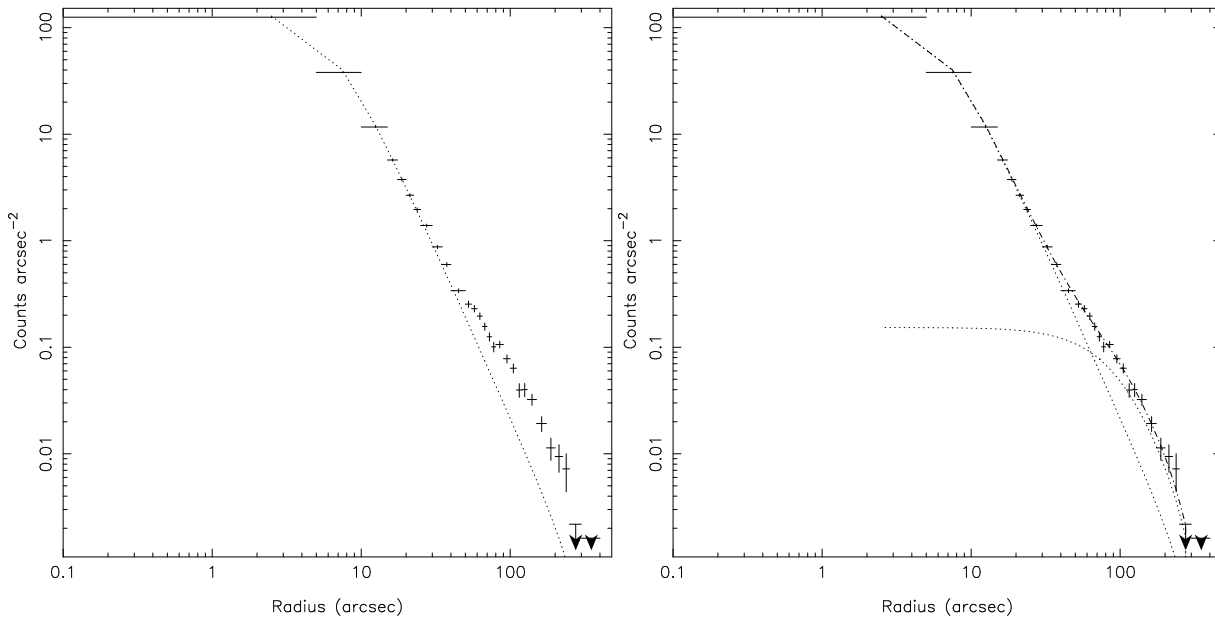
Figure 12. Radial surface brightness profiles for the pn data in the 0.3–7 keV energy band. Left: single point-source model. Right: convolved β-model plus point source, with the joint best-fitting β-model parameters given in the text.
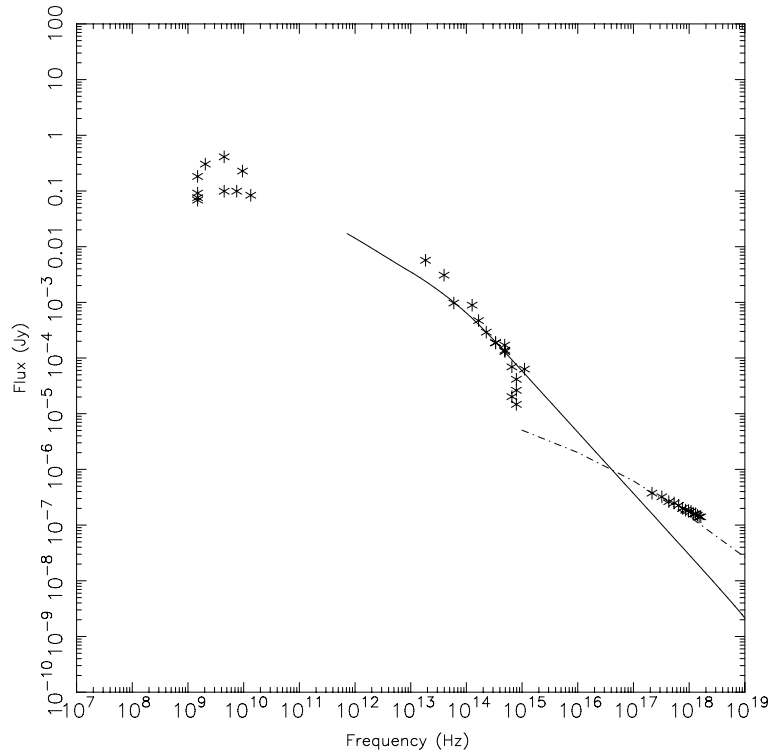
Figure 13. Radio-to-X-ray spectrum of NGC 6251 in the source frame, with model synchrotron and SSC fits to the data assuming a spherical geometry with emitting radius 5×10^{-4} pc. The solid line discussed shows the best-fitting synchrotron model, and the dot-dashed line shows the SSC emission expected. The electron spectrum is assumed to extend from $\gamma_{\min} \sim 20$ to $\gamma_{\max} \sim 4.5 \times 10^5$ with a number spectral index of $p = 2.4$, breaking by 1 at $\gamma \sim 600$. The model parameters are representative only and are poorly constrained due to the historical variability of the source and non-contemporaneous nature of the data. The model synchrotron emission shown is truncated at a frequency 10^{12} Hz, as self-absorption becomes important below this frequency.
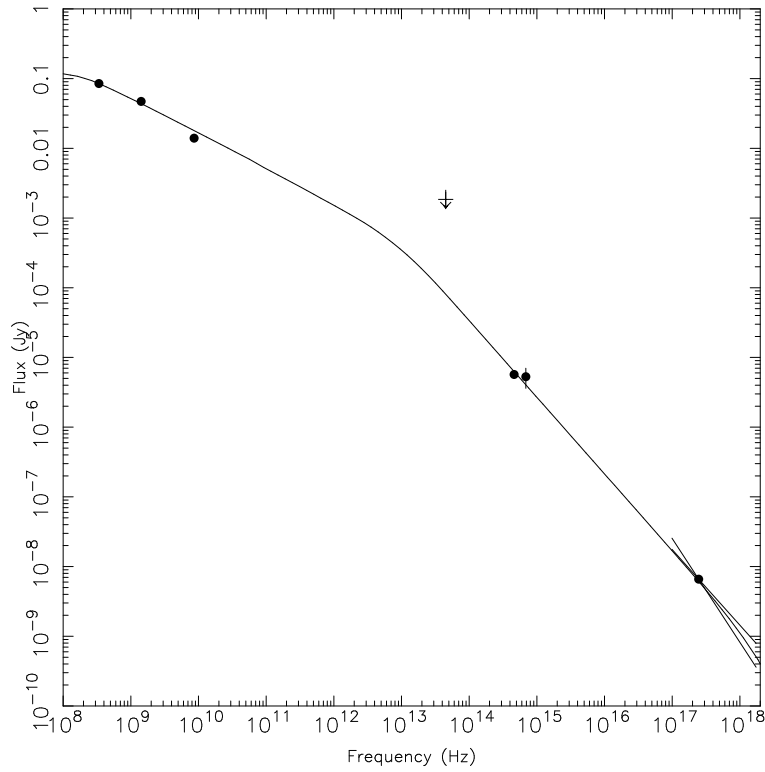
Figure 14. The radio to X-ray spectrum of the inner NGC 6251 jet. Plotted are data points from the radio, an infra-red upper limit from ISO (D. Tansley, private communication), the optical measurements (Werner 2002) and the X-ray data from *Chandra* (with 1-keV flux density and spectral errors). The solid line is the fitted synchrotron spectrum described in the text.
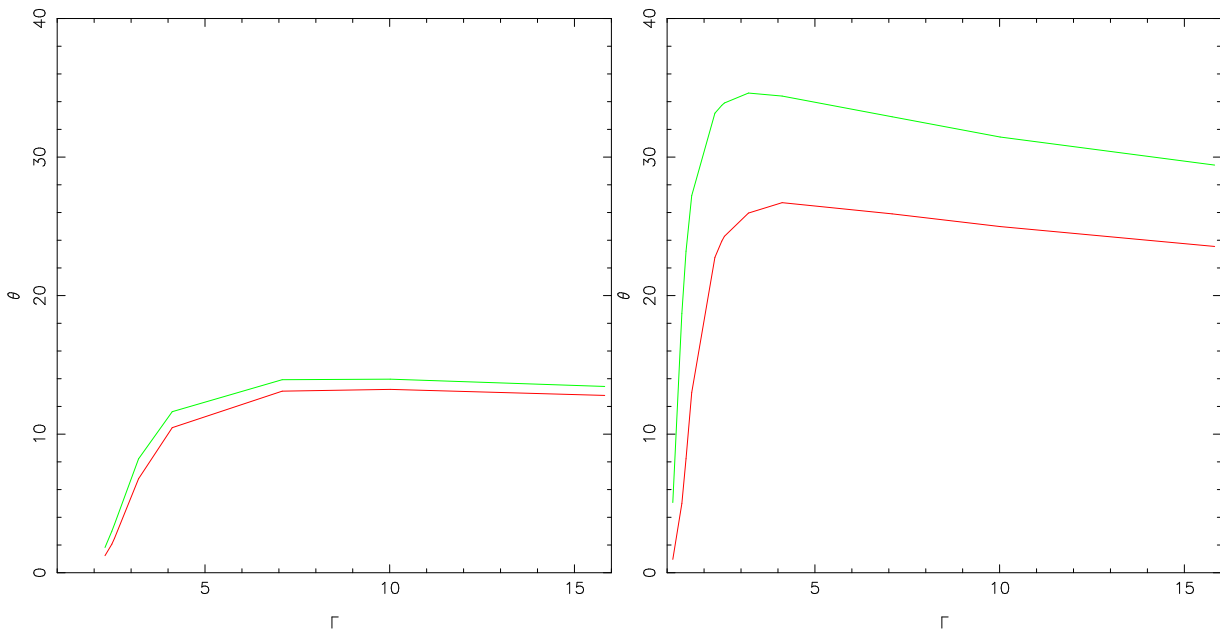
Figure 15. Constraints on the bulk Lorentz factor and angle to the line of sight for region 1 (left) and 2 (right) of the outer jet. The allowed region of parameter space (given the 1σ range on X-ray flux density) lies between the two lines.
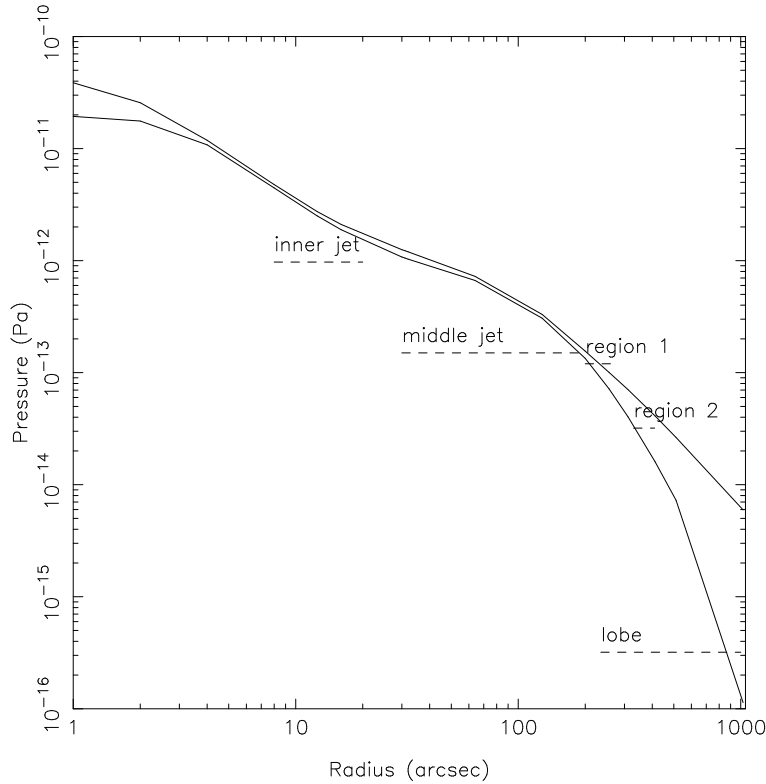
Figure 16. The thermal pressure (solid lines) and minimum radio pressure (dashed lines) in the radio components of NGC 6251 assuming no beaming and a jet in the plane of the sky (see Table 13). The solid lines show the total pressure in the thermal component, with the two lines reflecting the 1σ statistical uncertainties on pressure at each radius. Uncertainties on temperature are not included.
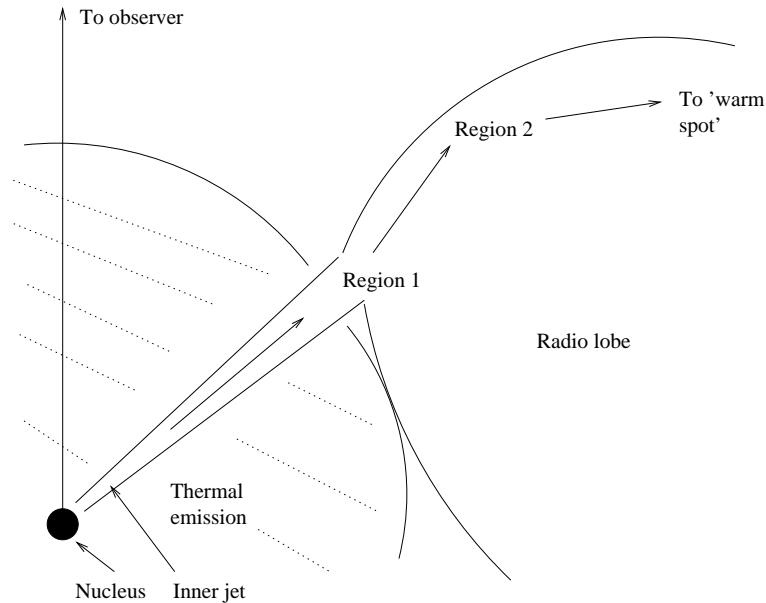
Figure 17. A sketch of a possible geometry for the N jet and lobe of NGC 6251 (not to scale). The observer is on the vertical axis, and the plane of the sky is perpendicular to the page. Thermal emission (sketched as a single contour of constant pressure; it should be assumed to fill the entire region) provides the pressure to confine the jet at small distances from the nucleus. The jet enters the lobe at region 1 and the change in conditions triggers particle acceleration, perhaps at a shock. The jet then bends at region 1 and interacts with the edge of the lobe at region 2 before continuing to feed the distant 'warm spot' at the end of the lobe. The discontinuity between the lobe and the thermal X-ray emission appears relatively sharp to a distant observer in this source geometry.

Table 1. *XMM-Newton* observed 0.15–10 keV count rates in a source-centred circle of radius 35 arcsec, together with nominal count rates above which pileup becomes important (as defined in the *XMM-Newton* Users' Handbook)

Camera	Total exposure time (ks)	Count rate (cts s^{-1})	Pile up threshold (cts s^{-1})
MOS1	23.7	0.556 ± 0.005	0.7
MOS2	24.7	0.574 ± 0.005	0.7
pn	8.1	1.973 ± 0.016	8

Table 2. VLA observations of NGC 6251 used in the analysis

Proposal ID	Date	Freq. (GHz)	Bandwidth (MHz)	Duration (h)	Config.	Map resn (arcsec)	Ref.
VJ38	1985 Apr 08	1.665	2×50	5.0	B	3.0×2.8	1
AK153	1986 Aug 20	1.452	25	2.8	B	4.9×3.7	
AZ032	1987 Aug 28	333	64×0.05	7.0	A	4.0×4.0	4
AZ35	1987 Dec 27, 1988 Jan 09	333	64×0.05	5.0	B	19×12	
VJ49	1988 Nov 20	1.665	2×50	11.6	A	1.3×1.1	2
AP0001	1990 Jun 27	8.427	7×3.125	3.3	BnA	0.77×0.58	
AM322	1991 May 09	8.415	2×50	1.2	D	8.7×7.7	
AB746	1995 Aug 15	1.387	32×0.4	3.0	A	1.7×1.2	3

References are (1) Jones et al. (1986) (2) Jones & Wehrle (1994) (3) Werner (2002) and Werner *et al.* (in prep.) (4) Birkinshaw *et al.*, in prep. The resolutions quoted are major axis × minor axis (FWHM) of the elliptical Gaussian restoring beam. The duration quoted is the time spent on source.

Table 3. *Chandra* and *XMM-Newton* best-fitting spectral parameters

Observation	Inner Extraction Radius	Outer Extraction Radius	Component	Parameters	Normalization
Chandra/ACIS-S	0.492 arcsec	1.23 arcsec	Power Law	$\Gamma = 1.67 \pm 0.06$	$(9.28^{+0.36}_{-0.33}) \times 10^{-4}$
			Thermal	$kT = 0.20 \pm 0.08$ keV; Abundance = 0.35 (frozen)	$(1.04 \pm 1.22) \times 10^{-4}$
	0.492 arcsec	35 arcsec	Power Law	$\Gamma = 1.69 \pm 0.09$	$(9.71 \pm 0.37) \times 10^{-4}$
			Thermal	$kT = 0.59 \pm 0.05$ keV; Abundance = 0.35 (frozen)	$(1.81 \pm 0.26) \times 10^{-4}$
XMM-Newton	0 arcsec	35 arcsec	Power Law	$\Gamma = 1.88 \pm 0.01$	MOS1 = $(1.20 \pm 0.02) \times 10^{-3}$; MOS2 = $(1.22 \pm 0.02) \times 10^{-3}$; pn = $(1.27 \pm 0.02) \times 10^{-3}$
			Thermal	$kT = 0.58 \pm 0.03$ keV; Abundance = 0.35 (frozen)	MOS1 = $(4.87 \pm 3.93) \times 10^{-5}$; MOS2 = $(6.41 \pm 4.06) \times 10^{-5}$; pn = $(2.07 \pm 0.28) \times 10^{-4}$

The thermal abundance was fixed at 0.35 solar, and the intrinsic absorption (in excess of the Galactic value) fixed at 4.50×10^{20} atoms cm^{-2}. Uncertainties are 90 per cent for one parameter of interest (i.e., $\chi^2_{min} + 2.7$). The *XMM-Newton* parameters quoted are for the 3σ GTI-filtering method defined in Section 3.2. The parameters derived with the other *XMM-Newton* GTI-filtering methods are consistent with those quoted here.

Table 4. Summary of *XMM-Newton* Exposures and Counts After GTI-Filtering

GTI filtering applied	MOS1			MOS2			pn		
	Exposure	2–10 keV Source Counts	5.5–7.5 keV Source Counts	Exposure	2–10 keV Source Counts	5.5–7.5 keV Source Counts	Exposure	2–10 keV Source Counts	5.5–7.5 keV Source Counts
Conservative	26.4 ks	4,041	325	27.5 ks	4,041	330	15.8 ks	6,861	868
3σ (from high-energy light curves)	43.2 ks	6,670	553	43.0 ks	6,472	601	38.1 ks	18,216	2503
3σ (from low-energy light curves)	43.9 ks	6,789	544	43.7 ks	6,599	627	39.5 ks	19,179	2701

Table 5. Significance of *XMM-Newton* Fe-line addition

GTI filtering applied	MOS1+MOS2	pn	MOS1+MOS2+pn
Conservative	100%	16.9%	87.2%
3σ (from high-energy light curves)	100%	17.0%	36.0%
3σ (from low-energy light curves)	100%	14.8%	9.0%

Percentages quoted are the probability of achieving a greater F by chance.

Table 6. Key spectral parameters after fitting Fe Kα line to the *XMM-Newton* data

GTI filtering applied	MOS1+MOS2	pn	MOS1+MOS2+pn
Conservative	$\Gamma = 1.77^{+0.15}_{-0.07}$	$\Gamma = 1.95^{+0.17}_{-0.12}$	$\Gamma = 1.87^{+0.13}_{-0.08}$
	E = N/A	E = 6.4 keV (pegged)	E = 6.51 keV (pegged)
	σ = N/A	$\sigma = 0.76 \pm 0.59$ keV	$\sigma = 4.02 \times 10^{-8}$ keV ($\pm$ unconstrained)
	norm = 0	norm = $(7.61^{+9.42}_{-7.61}) \times 10^{-6}$	norm = 6.52×10^{-7} ($\pm$ unconstrained)
3σ (from high-energy light curves)	$\Gamma = 1.84^{+0.16}_{-0.09}$	$\Gamma = 1.86^{+0.11}_{-0.04}$	$\Gamma = 1.85^{+0.09}_{-0.04}$
	E = N/A	$E = 6.83^{+0.95}_{-0.62}$ keV	$E = 6.90 \pm 3.29$ keV
	σ = N/A	$\sigma = 0.56^{+0.94}_{-0.54}$ keV	$\sigma = 0.51^{+1.93}_{-0.51}$ keV
	norm = 0	norm = $(4.46^{+5.02}_{-4.46} \times 10^{-6})$	norm = $(2.45^{+2.69}_{-2.45} \times 10^{-6})$
3σ (from low-energy light curves)	$\Gamma = 1.84^{+0.16}_{-0.09}$	$\Gamma = 1.87^{+0.11}_{-0.05}$	$\Gamma = 1.85^{+0.09}_{-0.04}$
	E = N/A	$E = 6.49 \pm 0.64$)	$E = 6.46^{0.13}_{-0.45}$
	σ = N/A	$\sigma = 0.38 \pm 0.26$	$\sigma = 1.77^{+9.71}_{-1.77} \times 10^{-2}$
	norm = 0	norm = $(3.98^{+6.02}_{-3.98} \times 10^{-6})$	norm = $(1.60^{+1.04}_{-1.60} \times 10^{-6})$

Uncertainties are 90 per cent for one interesting parameter (i.e., $\chi^2_{\min} + 2.7$).

Table 7. χ^2 results for fitting a constant count rate to the *XMM-Newton* and *Chandra* data sets with 3,000 second time bins. The *XMM-Newton* GTI filtering was identical to that of Gliozzi et al. (2004).

Observatory	Camera	Energy range (keV)	Average Count Rate (cts s^{-1})	χ^2 / dof	Null hypothesis probability
XMM-Newton	MOS1	0.8–10	0.42	8.45/13	0.82
	MOS2		0.43	15.29/13	0.29
	pn		1.17	22.35/13	0.05
	MOS1+MOS2+pn		2.03	26.07/12	0.01
Chandra	ACIS-S	0.3–10	0.68	13.37/16	0.65

Table 8. Long-term X-ray variability history of NGC 6251

Date	Observatory	2–10 keV PL-only luminosity	Photon Index	Reference
1991 March	*ROSAT*	$(1.8 \pm 0.5) \times 10^{42}$	$2.0^{+0.6}_{-0.5}$	Birkinshaw & Worrall (1993)
1994 October	*ASCA*	$(1.7 \pm 0.1) \times 10^{42}$	$2.11^{+0.16}_{-0.19}$	Turner et al. (1997)
2000 September	*Chandra*	$(4.3 \pm 0.4) \times 10^{42}$	1.76 ± 0.16	Guainazzi et al. (2003)
2001 July	*BeppoSAX*	$(7.1 \pm 0.6) \times 10^{42}$	$1.70^{+0.12}_{-0.16}$	Guainazzi et al. (2003)
2002 March	*XMM-Newton*	$(5.1 \pm 0.1) \times 10^{42}$	1.88 ± 0.01	Present work
2003 November	*Chandra*	$(6.1 \pm 0.2) \times 10^{42}$	1.67 ± 0.08	Present work

All luminosities quoted are unabsorbed. For *ROSAT*, the observed spectrum has been extrapolated to the 2–10 keV energy range. The errors quoted are statistical, i.e., 1σ.

Table 9. VLBI flux density estimates for the radio core and parsec-scale jet at several epochs and frequencies

Frequency	Date	Core flux density (Jy)	Jet flux density (Jy)	Total flux density (Jy)	Reference
1.6 GHz	1983 March	0.29	0.24	0.53	Jones et al. (1986)
	1985 April	0.21 ± 0.03	0.12 ± 0.02	0.33 ± 0.04	Present work
	1988 November	0.42 ± 0.03	0.09 ± 0.01	0.51 ± 0.04	Present work
	2000 May	0.31 ± 0.02	0.10 ± 0.01	0.41 ± 0.02	Present work
2.3 GHz	1980 February	0.25	0.40	0.65	Jones et al. (1986)
5.0 GHz	1981 December	0.35	0.54	0.89	Jones et al. (1986)
	2000 May	0.38 ± 0.04	0.13 ± 0.01	0.51 ± 0.05	Present work
8.4 GHz	2000 May	0.38 ± 0.04	0.13 ± 0.01	0.51 ± 0.05	Present work
10.7 GHz	1978 May	0.59	0.30	0.89	Cohen & Readhead (1979), Jones et al. (1986)
15 GHz	2000 May	0.39 ± 0.04	0.11 ± 0.01	0.50 ± 0.05	Present work

Table 10. Multi-epoch archival *HST* nuclear flux densities

Instrument	Filter	Date	Exposure time (seconds)	Pivot wavelength (Å)	Flux density (μJy)
WFPC2	F555W	1994 February 21	70	5442	171.56 ± 5.82
WFPC2	F555W	1995 June 28	800	5442	182.18 ± 1.77
WFPC2	F814W	1995 June 28	720	8002	244.95 ± 2.66
WFPC2	F814W	1996 September 13	1000	8002	248.38 ± 2.27
FOC	F342W	1991 May 12	1196	3403	34.56 ± 0.41
FOC	F342W	1993 September 30	2246	3403	19.36 ± 0.22
FOC	F342W	1996 February 19	1196	3403	54.64 ± 0.45
FOC	F410M	1993 September 30	1676	4088	26.70 ± 0.80
FOC	F410M	1996 February 19	1315	4088	91.22 ± 1.34

The quoted values have been dereddened assuming that the optical extinction to NGC 6251 is the sum of both the measured Galactic and intrinsic absorptions

Table 11. X-ray and radio flux densities and ratios for the kiloparsec-scale and parsec-scale jets

Component	1 keV X-ray flux density (Jy)	Radio flux density (Jy) (frequency)	Ratio ($\times 10^{-6}$)
Inner (kiloparsec-scale) jet	1×10^{-8}	3.1×10^{-2} (8 GHz)	0.32
Core power law / pc-scale jet	6.2×10^{-7}	~ 1 (5 GHz)	0.62

Table 12. X-ray-to-radio flux density ratios for a selection of FRI type radio galaxies

Source	1-keV X-ray to 8-GHz radio flux density ratio ($\times 10^{-6}$)	Reference
NGC 6251	0.32	Present Work
3C 66B	0.13	Hardcastle, Birkinshaw, & Worrall (2001)
3C 31	0.24	Hardcastle et al. (2002b)
Cen A	0.07–9.7 (various knots)	Hardcastle et al. (2003)
NGC 315	0.083	Worrall, Birkinshaw, & Hardcastle (2003)
3C 296	0.069	Hardcastle et al. (2005)

The X-ray and radio measurements are over the X-ray-detected regions of the jet.

Table 13. Minimum and thermal pressures in radio components of NGC 6251

Region	Minimum pressure (Pa)	Range (arcsec)	Inner p (Pa)	Outer p (Pa)
Inner jet (optical)	9.7×10^{-13}	8–20	$4.1^{+0.3}_{-0.2} \times 10^{-12}$	$11.0^{+0.9}_{-0.6} \times 10^{-13}$
Middle jet	1.5×10^{-13}	30–200	$7.8^{+0.9}_{-0.8} \times 10^{-13}$	$1.3^{+0.1}_{-0.1} \times 10^{-13}$
Outer jet region 1	1.4×10^{-13}	200–265	$1.3^{+0.1}_{-0.1} \times 10^{-13}$	$7.2^{+1.4}_{-1.5} \times 10^{-14}$
Outer jet region 2	3.2×10^{-14}	330–410	$4.3^{+1.4}_{-1.6} \times 10^{-14}$	$2.5^{+1.2}_{-1.3} \times 10^{-14}$
N lobe	3.2×10^{-16}	235–1000	$9.4^{+1.3}_{-1.4} \times 10^{-14}$	$2.5^{+3.9}_{-2.2} \times 10^{-15}$

Pressure for inner jet is calculated from the count density from the combination of the small- and large-scale β-model fits, assuming $kT = 0.59$ keV. Other pressures are calculated using the large-scale component only, assuming $kT = 1.7$ keV.